

University of Alberta

**Mechanical and Corrosion Properties of
Particle-Reinforced Polymer Composite Coatings**

by

Siaw Ling Lim



A thesis submitted to the Faculty of Graduate Studies and Research in partial fulfillment
of the requirements for the degree of Master of Science

in

Chemical Engineering

Department of Chemical and Materials Engineering

Edmonton, Alberta, Canada

Spring 2004



Library and
Archives Canada

Bibliothèque et
Archives Canada

Published Heritage
Branch

Direction du
Patrimoine de l'édition

395 Wellington Street
Ottawa ON K1A 0N4
Canada

395, rue Wellington
Ottawa ON K1A 0N4
Canada

Your file *Votre référence*
ISBN: 0-612-96514-7
Our file *Notre référence*
ISBN: 0-612-96514-7

The author has granted a non-exclusive license allowing the Library and Archives Canada to reproduce, loan, distribute or sell copies of this thesis in microform, paper or electronic formats.

L'auteur a accordé une licence non exclusive permettant à la Bibliothèque et Archives Canada de reproduire, prêter, distribuer ou vendre des copies de cette thèse sous la forme de microfiche/film, de reproduction sur papier ou sur format électronique.

The author retains ownership of the copyright in this thesis. Neither the thesis nor substantial extracts from it may be printed or otherwise reproduced without the author's permission.

L'auteur conserve la propriété du droit d'auteur qui protège cette thèse. Ni la thèse ni des extraits substantiels de celle-ci ne doivent être imprimés ou autrement reproduits sans son autorisation.

In compliance with the Canadian Privacy Act some supporting forms may have been removed from this thesis.

Conformément à la loi canadienne sur la protection de la vie privée, quelques formulaires secondaires ont été enlevés de cette thèse.

While these forms may be included in the document page count, their removal does not represent any loss of content from the thesis.

Bien que ces formulaires aient inclus dans la pagination, il n'y aura aucun contenu manquant.

Canada

ABSTRACT

To date, little attention has been devoted to embedding nanoparticles into the polymer matrix to enhance the mechanical properties of the composite materials, while maintaining inherent corrosion resistance of the polymer. This thesis aims at contributing to the ongoing effort of understanding the mechanical and electrochemical properties of polymer and its composite coatings. In this thesis, polymer suspensions containing nanosized tungsten carbide or alumina particles are coated on steel substrate surfaces by spin coating method. The purpose of coating is to provide improved corrosion-erosion resistance of polymer by embedded nanoparticles.

The mechanical and electrochemical properties of coatings were studied using Vickers microhardness test, scratch test, Taber abrasion test, erosion-corrosion test and dc polarization test. It was found that the extent of the improvement depended largely on the particle size, particle content and homogeneity of particle distribution in the polymer matrix and interface bonding between the particles and polymers. The results indicated that the addition of nanoparticles into the polymer phase enhanced microhardness, scratching resistance and abrasion resistance of the composite coatings without sacrificing the corrosion resistance of the polymer itself. Current study further demonstrated that polymer-nanoparticle composite coatings could be a viable avenue to tune materials properties for the desired applications.

TABLE OF CONTENTS

CHAPTER 1 INTRODUCTION	1
CHAPTER 2 LITERATURE REVIEW	4
2.1 INTRODUCTION	4
2.2 CORROSION - EROSION	5
2.3 COATING MATERIAL AND METHODS	7
2.3.1 Soft Coatings	7
2.3.2 Effect of Fillers	9
2.3.3 Effect of Transferred Film	9
2.3.4 Effect of Testing Conditions	10
2.3.5 Effect of Filler Content	10
2.3.6 Effect of Type of Fillers	10
2.3.7 Filler Affecting Polymer Microstructure	11
2.3.8 Wear Mechanism of Polymer	11
2.4 HARD COATINGS	13
2.4.1 Welding Overlay	13
2.4.2 Chemical Vapor Deposition (CVD)	15
2.4.3 Physical Vapor Deposition (PVD)	17
2.4.4 Thermal Spray	18
2.4.5 Electrochemical Deposition	20
2.4.6 Sol-Gel	21
2.4.7 Electrophoretic Deposition (EPD)	21
2.5 NANOSIZE PARTICLES	24
2.5.1 Materials Selection	25
2.5.2 Yield Stress of Nanostructured Materials	26
2.5.3 Sintering Temperature of Nanosize Particles	26
2.5.4 Superplasticity	26
2.6 APPLICATION OF NANOSTRUCTURED PARTICLES	27
CHAPTER 3 EXPERIMENTAL PROCEDURE	29
3.1 MATERIALS	29
3.1.1 Substrate	29

3.1.2 Polymer	29
3.1.3 Powder	29
3.1.4 Silica sand particles.....	29
3.1.5 Chemicals.....	30
3.2 EXPERIMENTAL PROCEDURE	30
3.2.1 Preparation of Powders	30
3.2.2 Preparation of Polymer Suspension.....	31
3.2.3 Spin Coating.....	32
3.2.4 Taber Abrasion Test	33
3.2.5 Vickers Microhardness Tester.....	34
3.2.6 Universal MicroTriboscope Tester.....	35
3.2.7 Abrasion Resistance.....	36
3.2.8 Electrochemical Method – Potentiodynamic Polarization Scan.....	37
3.2.9 Erosion-Corrosion Test	39
CHAPTER 4 RESULTS & DISCUSSION.....	43
4.1 MORPHOLOGY OF COATINGS	43
4.1.1 Coatings after Heat Treatment	43
4.1.2 Cross-section of Coated Sample	45
4.2 MICROHARDNESS	46
4.3 SCRATCHING RESISTANCE	49
4.3.1 Scratching Resistance of Coatings.....	49
4.3.2 Friction Coefficient during Scratching	52
4.3.3 Effect of Particle Size on Scratching Resistance	53
4.3.4 Stick-slip Effect	54
4.3.5 Relationship between Scratching Resistance and Hardness	56
4.3.6 Mechanism of Deformation	56
4.3.7 Scratched Surface of Coatings	57
4.4 TABER ABRASION TEST.....	61
4.4.1 Abrasive Wear.....	61
4.4.2 Mechanism of Abrasive Wear.....	65
4.5 ELECTROCHEMICAL TEST	65

Potentiodynamic Polarization of Coatings.....65

4.6 EROSION-CORROSION TEST 71

 4.6.1 Volume Loss for Carbon Steel, Polymer and Polymer Composites71

 4.6.2 Comparison between GemThane and Xylan 181076

CHAPTER 5 CONCLUSIONS & RECOMMENDATIONS FOR FUTURE WORK 80

 5.1 CONCLUSIONS..... 80

 5.2 RECOMMENDATIONS FOR FUTURE WORK.....81

REFERENCES 82

LIST OF FIGURES

Figure 2-1 An electrochemical corrosion cell consists of an anode, cathode, electrical conductor and ion conductor.....	5
Figure 2-2 Polytetrafluoroethylene (PTFE).....	8
Figure 2-3 Wear deformation of polymer (extracted from Briscoe, 1981).....	12
Figure 2-4 Picture of the impingement of a solid particle on a polymer surface.....	12
Figure 2-5 Sequence of events taking place inside the reaction chamber during CVD process (extracted from Pierson, 1999).	16
Figure 2-6 Schematic of an electrophoretic deposition process. Positively charged particles migrate to the negatively charged electrode.....	22
Figure 3-1 Illustration of spin coating method. Excess suspension spins off during rotation, leaving a uniformly distributed coating.....	33
Figure 3-2 Schematics of coating layers on a substrate.....	33
Figure 3-3 Schematics of a typical indent.....	34
Figure 3-4 The geometry of the probe for scratch tests.....	35
Figure 3-5 Basic principle of scratch test.	36
Figure 3-6 Taber Abrasion Tester—Abraser Model 5130	36
Figure 3-7 Extrapolated polarization curves for anode and cathode reactions to obtain i_{corr} values.	38
Figure 3-8 Experiment setup for the erosion-corrosion test.	39
Figure 3-9 Details dimensions of the electrochemistry cell used in E-C test (Side view).....	40
Figure 3-10 Details dimensions of the sample holder used in E-C test.....	41
Figure 3-11 Plastic cover is used to seal the O-ring and sample holder together to prevent leakage as well as to keep the sample holder stationary during E-C test.	41
Figure 3-12 Irregular shape of sand particle used for E-C test is approximately 300 μm in size.	42
Figure 4-1 Optical micrograph of coatings: (a) polymer alone (b) 10 wt% 50 nm Al_2O_3 composite; (c) 10 wt% 300 nm Al_2O_3 composite; and (d) 10 wt% WC composite (dark area: WC clustered and light area: polymer).	45

Figure 4-2 Cross-section of 10 wt% WC composite coating.....	45
Figure 4-3 Microhardness measurements for polymer and its composite coatings at applied constant load of 50g	47
Figure 4-4 Effect of particle size on hardness of Al ₂ O ₃ composite coatings.	48
Figure 4-5 Scratching resistance for different coatings under progressive load.....	51
Figure 4-6 Scratching resistances of 300 nm and 50 nm Al ₂ O ₃ particles.....	54
Figure 4-7 Scratching resistance versus time at applied constant load.....	55
Figure 4-8 Relationship between scratching resistance and microhardness.....	56
Figure 4-9 Front view of the indenter during scratching.	57
Figure 4-10 SEM micrographs show the images of the scratch tracks on coatings under progressive load condition.	60
Figure 4-11 Wear rates of (a) Al ₂ O ₃ composite coatings and (b) nanostructured WC composite coatings obtained from Taber abrasion test.....	63
Figure 4-12 A unique “X” pattern of abrasion is produced by the rotary rub-wear action of the wheels. The abrasion marks are deeper in (a) polymer, and become less visible in 10 wt% Al ₂ O ₃ (b) and 20 wt% Al ₂ O ₃ (c) polymer composite coatings.	64
Figure 4-13 Combined action of loosen particles and abrasive wheel on composite coating surface during Taber abrasion test.....	65
Figure 4-14 Potentiodynamic curves for different coatings at (a) beginning (b) 2 hours later and (c) 24 hours later in 3 wt% NaCl solution.	68
Figure 4-15 Variation of corrosion potential of coatings with immersion time in 3 wt% NaCl.	70
Figure 4-16 Corrosion current density of composite coatings varies with time in 3 wt% NaCl.	70
Figure 4-17 Volume loss of polymer and its composites coatings in a simulated erosive and corrosive environment.....	73
Figure 4-18 Carbon steel surface covered with pits and grooves after E-C test.....	74
Figure 4-19 Wavy surface of 10 wt% Al ₂ O ₃ composite coating after twelve hours exposure in E-C test.....	75
Figure 4-20 Surface of 10 wt% WC composite coating after 12 hours exposure in E-C test. The surface is ‘smoother’ than that before E-C test.....	75

Figure 4-21 Weak bonding between protruded particles and polymer is detrimental to the composite coating. The protruded particles are likely to be removed from the coating surface due to the impact from impinging sand particles. 76

Figure 4-22 Pictures showing the adhesion failure joints between the coatings and substrates..... 78

Figure 4-23 Xylan 1810 coatings after 53 hours exposure in of E-C test. All the samples A, B, C and D were subjected to the same condition of preparation and E-C test. 79

LIST OF TABLES

Table 3-1 A summary of the physical and chemical properties of the sand particles.....	30
Table 3-2 A summary of nanoparticles in polymer suspension used in this study.	31
Table 4-1 Scratching resistance of the substrate and various coatings obtained under progressive load condition.	52
Table 4-2. Weight of GemThane polymer before and after E-C test.	77
Table 4-3. Weight of 10 wt% Al ₂ O ₃ in GemThane before and after E-C test.	77

LIST OF SYMBOLS

A_s	Width of scratch track (μm)
c	Constant (sec^{-1})
D	Length of diagonal line of indentation (μm)
d	Grain size (nm)
E	Activation energy (kJ mol^{-1})
E_{applied}	Sweeping potential range (mV)
E_{corr}	Corrosion potential (mV)
F	Faraday constant (96,490 C)
F_z	Applied normal load (g)
$F_{z,\text{max}}$	Maximum applied normal load (g)
H_v	Vickers microhardness ($\text{g}/\mu\text{m}^2$)
i	Measured current density (A/cm^2)
i_{corr}	Corrosion potential (A/cm^2)
k	Constant ($\text{MPa}\cdot\text{nm}^{1/2}$)
n	Number of mole of electron / mole of metal
P	Test load (g)
R	Gas constant ($8.314 \times 10^{-3} \text{ kJ mol}^{-1}\text{K}^{-1}$)
R_x	Scratching resistance (g)
s	Deposition rate (sec^{-1})
T	Deposition temperature (K)
β	Tafel slope (mV)
η	Potential difference (mV)
σ	Yield stress (MPa)
σ_0	Friction stress (MPa)
ρ	Density (g/cm^3)
ΔG	Gibbs energy (J/mol)

CHAPTER 1 INTRODUCTION

Any material will be damaged if it is exposed to severe environments such as corrosion or erosion in pipelines, swelling of polymer in solvents, degradation of concrete in sewage, etc. These deteriorating processes occur under various mechanisms. Most engineering metals are susceptible to corrosion by the same basic mechanisms, either attacked uniformly or through cracks (Bradford, 1993). Corrosion of engineering metals can be spontaneous and happened easily in the presence of water. In fact, corrosion is such a huge problem in industry that it can cause billions of dollars annually to replace corroded parts, or repaint metals to maintain corrosion protection. Undetected failure in corrosion and erosion could lead to serious accidents such as leakage in oil pipelines and explosions of reactors. The aftermaths include plant shutdowns, loss of production and low efficiency. Many corroded metals, especially nickel and chromium that are important in alloying cannot be recycled by any means.

In order to control both corrosion and erosion in metals, it is essential to envisage proper coatings that exhibit higher resistance to corrosion and erosion than metals. The coatings serve as a protective layer to protect the metals from contacting corrosive and wear environments. It is commonly accepted that a protective coating, whether metallic or ceramic, must form a compact barrier and have good adherence to the substrate so as to prevent the penetration of water and oxygen. However, defects within these coating materials are often inevitable. Hence, the performance of the coatings sacrifices unless a proper method is used to mitigate the defects. Other possible route to protect the substrate is to use organic coatings such as fluoropolymer. The strong C-F bonds in fluoropolymer provide an excellent resistance to corrosive chemicals, organic solvents and deterioration of protective films at an elevated temperature. Other desired properties of fluoropolymer coatings are low friction and abrasion, oil and water repellency and anti-fouling.

Many research efforts have been devoted to embedding particles into the polymer matrix to enhance the mechanical properties of the composite materials, while maintaining inherent corrosion resistance of the polymer. To date, little attention has been given to the study on the abrasive wear or electrochemical effect of embedded

nanoparticles, especially nanosize tungsten carbide particles in polymer matrix or coatings. By incorporating nanosize particles into the polymer matrix, the polymer composites may exhibit different characteristics than the pure polymer in terms of wear resistance (i.e. scratch resistance, abrasion resistance, erosion-corrosion resistance) and corrosion resistance. Such attempt may lead to discovery of the new coatings. Characterizing and testing the polymer-based composite coatings using available technology would help improve the overall performance of coatings.

With the new and improved deposition techniques emerging in today's technology, a wide range of ceramics and metallics can be coated on substrates using conventional routes such as physical or chemical vapor deposition, thermal spray and sol-gel process, whereas polymeric coatings can be applied more readily through spraying, brush painting or spin-coating. An ideal polymeric coating should be adhesive to hold the particle-particle and particle-substrate together, yet corrosion resistant. Depending on deposition methods the quality of the coatings varies.

The objective of this thesis aims at contributing to the ongoing effort of understanding the hardness and wear resistant of embedded nanoparticles in polymer phase. The main focus is on thorough characterization of the microstructure and mechanical properties of polymer composite coatings. Additionally, the fracture mechanisms were studied using SEM, allowing to predict how the coated systems will perform in service.

The polymer composite tested consists of nanosize particles uniformly dispersed in the polymer solution with the aid of an ultra-sonic dismembrator. Particle sizes for Al_2O_3 are 50 nm and 300 nm, and for tungsten carbide (WC) it is 300 nm. The polymer composites were prepared to have different particle content and coated on the substrate using a spin-coating method. The mechanical and electrochemical properties of these coatings were determined using Triboscope, microhardness, Taber abrasion test, and electrochemical methods. Simulated erosion tests were also performed under a corrosive environment to determine the suitability of the usage of polymer composites coatings in a slurry pipeline system.

The outline of the thesis is as follows: Chapter 2 reviews some commonly used deposition techniques, including soft coatings such as polymer and its composite, and

hard coatings such as welding overlay, physical vapor deposition (PVD), chemical vapor deposition (CVD), thermal spray, electrochemical deposition, sol-gel and electrophoretic deposition (EPD). Chapter 2 also covers discussions on some properties of the nanoparticles which are related to the current thesis work.

Chapter 3 describes the detailed experimental procedures for particle enhanced polymer composite coatings. The principles governing the apparatus used in this thesis were also presented in Chapter 3.

Chapter 4 discusses the results of the role of particle reinforcement on composite coatings in terms of their morphology, scratch and abrasive wear behavior, electrochemical property and erosion-corrosion resistance.

Conclusions derived from this thesis work and recommendations for future work are given in Chapter 5.

CHAPTER 2 LITERATURE REVIEW

2.1 INTRODUCTION

The demands for increasing mechanical and chemical loads on the material used for a variety of industries have probably grown at a faster pace than the required number of materials available to meet the requirement. Although a great deal of efforts has been devoted to producing new materials with improved properties, there exists a limit to the protection provided by improving the properties of bulk materials alone. Therefore, coatings have played an important role in protecting metals from severe environmental attacks either mechanically or chemically (Dahotre et al., 2001).

Selection of coating materials can range from advanced ceramics to polymer nanocomposites, depending on the purpose of end-users. Methods of coating will vary according to the selection of coating materials. It is highly desirable that coatings can be applied using a simpler and more flexible technique than dealing with the conventional coating methods.

In general, most organic and inorganic materials can now be applied to any metallic surface as coatings. Organic coatings use a complex mixture of polymers, fluid carriers, pigments and additives whereas inorganic coatings comprise of metallic and ceramic materials as protection against corrosion and erosion (Taylor, S.R., 2001). Common ceramics used in coatings are oxides, carbides, nitrides, borides and silicides. These refractory materials possess wear- and corrosion-resistance at high temperatures and their applications are widespread, ranging from aerospace, automotive, incineration to power generation industries. Oxide coatings are mostly used in the fuel-cell due to their low thermal conductivity, thereby acting as a good thermal barrier. Carbides and nitrides are well-known for their great hardness and high melting point. These characteristics have resulted in the extensive use of carbides as cutting tools and for wear-resistant surfaces, whereas nitrides are widely used in extreme conditions such as hot-working tool steel for die-casting services. Other ceramics such as borides and silicides also find their usage as components in atomic reactors and space shuttles, respectively (Dahotre et al., 2001).

Due to their unique features, spreading polymer nano-composites and electrophoretic deposition (EPD) have become a subject of intense research as favorite coating methods. Both methods have unique features of easy accessibility and versatility that cannot be achieved by other existing deposition processes such as physical vapor deposition (PVD), chemical vapor deposition (CVD), thermal spray and sol-gel coatings. The accessibility and versatility of these two methods to coat on irregular objects and inner surfaces are highly distinguished from the other processes which are time consuming and cumbersome in operation.

2.2 CORROSION - EROSION

To develop coatings for corrosion/erosion protection, it is desirable to understand basics involved in a corrosion-erosion system. In general, a corrosive system consists of an anode and a cathode, electrical connection and a liquid medium for ions transportation (e.g. water). The absence of any one of these elements will prevent corrosion. For aqueous corrosion, the corrosive environment can be illustrated as an electrochemical corrosion cell, see Figure 2-1.

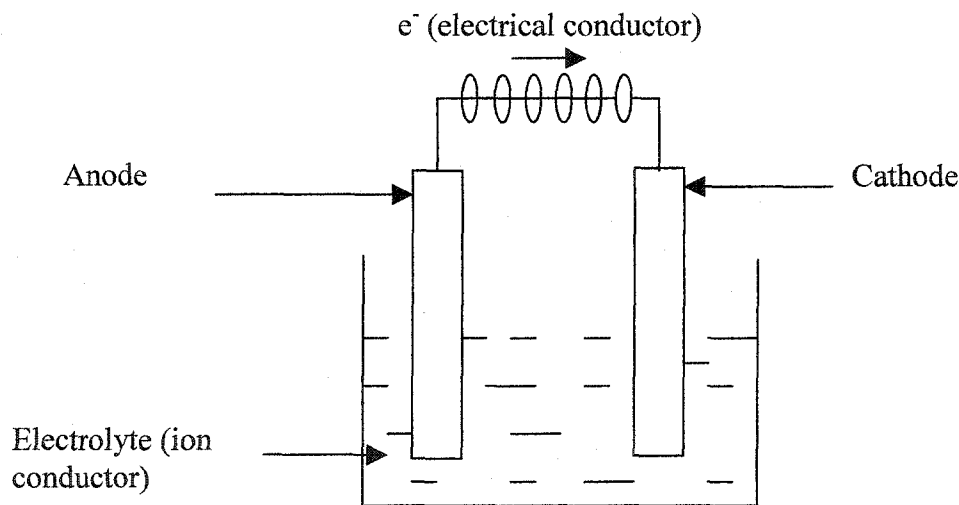


Figure 2-1 An electrochemical corrosion cell consists of an anode, cathode, electrical conductor and ion conductor.

At anode, metal corrodes and dissolves into the solution as metal ions. This reaction is known as oxidation.



The electrons produced do not flow into the solution but migrate through the electronic conductor to the cathode. Those electrons produced at anode were consumed at the cathode by some reducible species in the electrolyte. The valence of the reactant at cathode is reduced and this is called reduction process. The most common reduction process in neutral or basic solutions is:



The driving force for corrosion is the change in Gibbs energy (J/mole), ΔG , which is the change in Gibbs energy of the corrosion cell. The metals will try to lower their energy by giving up electrons to reach a greater thermodynamic stability. ΔG must be always negative for a spontaneous reaction. In corrosion measurement, the ΔG is defined as follow:

$$\Delta G = -nFE_{\text{cell}} \quad (2.3)$$

where n = number of mole of e^- per mole of metal involved

F = Faraday constant (96,490 C)

E_{cell} = potential difference developed by the corrosion cell (Volts)

E_{cell} can be determined easily from the corrosion cell. However, the E_{cell} can not be used to predict the corrosion rate because a large cell potential does not necessarily mean that the metal will corrode badly. The parameter that determines a metal's susceptibility to corrosion attack is the corrosion current density, i (A/area) in the corrosion cell.

$$\text{Corrosion rate} = i / nF \quad (\text{mol/area.time}) \quad (2.4)$$

In addition to these four basic corrosion components, a wear environment will accelerate corrosion. Wear is manifested in several forms, depending on the environment of operation. Erosion wear is caused by impingement of solid particles, small drops of liquid or gas on an object. In a slurry pipeline, both erosion and corrosion are inevitable. The surfaces of the pipe in this case are damaged not only by the impact of solid particles

but also by chemical or electrochemical corrosions and interaction between erosion and corrosion (Neville and Hodgkiess, 1997).

One method to minimize the corrosion in an erosive environment is by surface coatings. In this case, the coating should provide barriers to at least one of the corrosive species. The determining factors of a successful coating include surface preparation, coating application methods and service environment, in addition to considering the coating material itself (Taylor, 2001).

2.3 COATING MATERIAL AND METHODS

2.3.1 Soft Coatings

Polymer and polymer composites are widely used as coatings because of their self-lubricating properties, high inertness, great electrical resistance, excellent corrosion resistance, high capacity for damping vibrations, light weight and low cost (Bhushan and Gupta, 1991). Many polymer coatings are a blend of different types of polymers, including PTFE, polyamide, polyethylene, polyimide, phenolic, nitrile, fluoroelastomer, etc. Usually a polymer-polymer interface exhibits a higher tolerance to abrasive particles because some particles would be embedded into the polymers.

Polymers are divided into thermoplastics and thermosets based on their distinct characteristics at elevated temperatures and production processes. Thermoplastics solidify upon cooling and can be melted repeatedly whereas thermosets become cross-linked upon cooling and cannot be restored to initial flowability with subsequent heating. Thermoplastics can be amorphous or crystalline. Majority of thermoplastics used for tribological applications are of crystalline structures. Of all the plastics, PTFE has been used extensively either in its pure form or as fillers. PTFE has the lowest friction coefficient than any other known polymers.

PTFE belongs to fluoro carbon family, with fluorine atoms substituting hydrogen atoms in olefins. Figure 2-2 shows the chemical structure of a PTFE monomer. The carbon-carbon bonds, which form the backbone of the PTFE chain, and the carbon-fluorine bonds are extremely strong and are the key contributors to its outstanding properties (Gangal, 2001). Strong carbon-fluorine covalent bond in PTFE is the main

reason for its extreme chemical stability. The carbon-fluorine covalent bond also reduces the surface energy, resulting in low coefficient of friction and nonstick properties. Below 20°C, PTFE exists in highly crystalline form.

The transition point from partly crystalline to amorphous structure begins at about 330°C. This group of plastics is probably the most employed polymers for friction and wear protection applications in microelectronic industries. In fact, half of PTFE product is consumed in electrical applications with mechanical and chemical applications sharing equally the other half. The PTFE family plastics show great chemical inertness, dielectric properties, heat resistance and low friction coefficients.

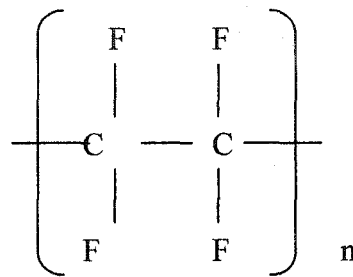


Figure 2-2 Polytetrafluoroethylene (PTFE)

One of the controversial objectives about polymers is their physical absorption of liquids. Absorption of a liquid is referred to as the liquid dissolving in the polymer. Submicroscopic voids exist between the polymer molecules, providing the space for the liquid. The absorption of the liquid by a polymer is indicated by a slight weight increase and sometimes by discoloration (Gangal, 2001). Common acids or bases are not absorbed by PTFE up to 200°C. Aqueous solutions are seldom absorbed at atmospheric pressure. Even the absorption of organic solvents by PTFE is marginal, partially resulting from the low wettability of PTFE. The polymer does not suffer losses of mechanical or bulk electrical properties unless it is subjected to severely fluctuating conditions.

Despite of their many outstanding properties, neat polymers have inherent weaknesses when compared with metals. When subjected to prolonged exposure in various liquids, for example, polymers are known to swell. Polymers have a much lower thermal conductivity than metals. Therefore, they are less able to dissipate frictional heat

generated at rubbing interfaces. The accumulated heat at the surface and in the subsurface layer may accelerate mechanochemical degradation and thermal decomposition of the polymers that exposed to abrasive conditions. These effects become much more pronounced in high elasticity polymers such as styrene-butadiene rubber (SBR). As a result, a sticky layer is often formed within the surface regions due to polymer degradation. In an erosion environment, this layer is easily torn away from the surface by the impact of abrasive particles. As the processes continue, the materials eventually will be worn off under the action of microcutting/microploughing (Zhang et al., 1995). For relatively higher strength and hardness polymers, such as polyurethane (PU), the mechanochemical degradation and thermal decomposition are less severe.

2.3.2 Effect of Fillers

Due to the shortcomings of neat polymers, fibers, fillers and additives are added into polymer matrix to reinforce their mechanical properties. Extensive work related to tribological behaviors of polymer composites has been done by Tanaka et al., (1982); Bahadur and Gong, (1990); Wang, (1996); Xu and Mellor, (2001). These authors have shown that adding certain amount of filler particles can improve the hardness and wear resistance, of the polymer composites. However, there are cases where the embedded particles could not enhance the mechanical properties of the polymers. The performance of the polymer composites strongly depends on the type of tests, type of reinforcements, and also the interaction and adhesion between the phases (Xu and Mellor, 2001).

2.3.3 Effect of Transferred Film

When polymer is rubbed against an abrasive surface, the adhesive forces between the sliding interfaces will cause cohesive failure of the polymer near the interface and the polymer is transferred onto the counterface (Briscoe, 1981). The transferred polymer to the counterface is known as transferred film. In fact, wear behavior of polymers is normally related to the transferred film on the counterface. Most researchers indicate that the formation of a transferred film on the counter part steel surface during friction processes is one of the most important factors to the success of improving wear

resistance. If the transferred film is adhered strongly to the counterface, the wear is reduced, often by large factors.

2.3.4 Effect of Testing Conditions

As mentioned, testing condition has an important influence on the friction and wear processes of the polymer composites. If the transferred film is weakly attached to the counterface, it is easily detached from the counterface by repeated sliding of the polymer pin on the same tractions. Meantime, depending on the geometry and operating system of the apparatus, the transferred film would eventually displace from the tractions after the repeated sliding motion from the polymer pin. The detached film from the counterface would cause the polymer to transfer a new film on the same tractions. This effect is typical in a pin-on-disc configuration where more films are transferred to the counterface, resulting in a high wear rate. In confined or conforming contacts between the polymer and the counterface, the wear is reduced because the debris could not escape and back transfer may occur (Briscoe, 1985).

2.3.5 Effect of Filler Content

As studied by Wang et al.(1996), polyetheretherketone (PEEK) filled with ZrO_2 can either produce lower or higher wear rate based on the proportion of ZrO_2 particles in the PEEK. The filled PEEK exhibits a sharp decrease in the wear rate in comparison with the pure PEEK. The wear rate of the filled PEEK reaches a minimum for a ZrO_2 content of 7.5 wt%. Above 7.5 wt% ZrO_2 , the wear rate begins to climb up linearly with further increasing ZrO_2 content. Similar trend is also observed by Li et al. (2002), for nanometer ZnO in PTFE.

2.3.6 Effect of Type of Fillers

In fact, different type of fillers can affect the frictional coefficient of the polymer composites significantly. Fillers such as aluminium, plumbum sulfide (PbS), yttrium(203), iron, copper and nickel could increase the frictional coefficient of PTFE composites as compared with that of the pure PTFE (Gong et al., 1990). On the other

hand, other fillers such as tungsten, tin, selenium and boron could reduce the frictional coefficient of the PTFE composites in relative to the pure PTFE.

2.3.7 Filler Affecting Polymer Microstructure

The added fillers into a polymer matrix often affect the microstructure of the polymer, resulting in different chemical and mechanical properties. Dated back to 1990, Gong et al, used XRD to analyze the crystalline structure of the pure PTFE and PTFE composites. By adding metal powders to the pure PTFE, the amorphous region in the PTFE composite reduced remarkably. Recently, Li et al. (2002), in their article showed SEM cross section morphologies of pure PTFE and nanometer ZnO filled PTFE composite. Many long fibers distributed on the cross-section of pure PTFE, which were produced by large-scale destruction of the banded structure of PTFE when preparing the sample. However, no fibers were seen in nanometer ZnO filled PTFE composite under the same condition. The ZnO filler dramatically prevented the destruction of the banded structure of PTFE. The ZnO filler that distributed uniformly on the subsurface of PTFE composites could reduce the destruction of PTFE during friction process, which was also confirmed by Tanaka and Kawakami (1982).

2.3.8 Wear Mechanism of Polymer

The wear mechanisms of organic polymer were reviewed by Briscoe in 1981. Two general classes of polymer wear processes are cohesive wear and interfacial wear. Cohesive wear is the dissipation of frictional work which involves relatively large volumes close to the interface. This includes abrasion and erosive wears. The wear mechanisms are largely governed by the cohesive strength or toughness of the polymer.

Example of cohesive wear can be illustrated through the abrasive wear process, as shown in Figure 2-3. During the abrasive wear when harder surface is pressed into the softer surface, a plastic flow occurs on the softer surface around the asperity from the harder surface. By imposing a tangential motion, the soft polymer will be removed under the effects of microploughing, microcutting and microcracking. In addition, fatigue wear could also occur when the polymer surface is experiencing repeating stresses.

Consequently, the cohesive energy of the polymer and substrate will be weakened. Crack growth would be initiated in the subsurface and finally propagated into the surface layer (Zhang et al., 1995).

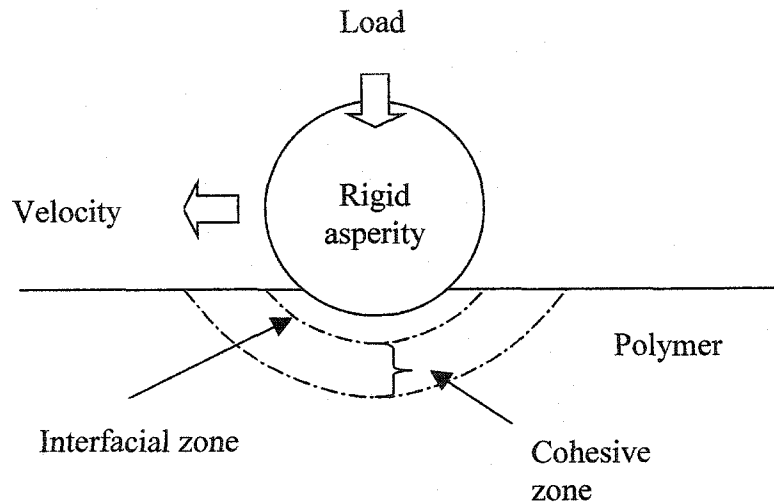


Figure 2-3 Wear deformation of polymer (extracted from Briscoe, 1981).

Another type of wear that is also related to cohesive wear of polymer, is erosive wear by solid particles and fluids. Erosion of polymer is resulted from the impingement of either solid particles or fluids. As a result from the impact of solid particles upon the polymer, part of the polymer surface is removed. The degree of erosion depends on the inherent property and history of the polymer, the shape and size of particles, and the impact velocity. Figure 2-4 below depicts the mechanism of erosion wear on a polymer surface.

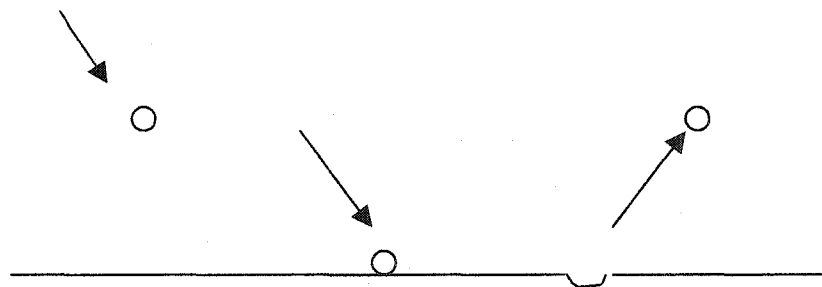


Figure 2-4 Picture of the impingement of a solid particle on a polymer surface.

Interfacial wear originates from dissipation of frictional energy at a much thinner region adjacent to the interface. The frictional energy is emanated from adhesive forces resulted from the contacting surfaces in a much smaller volume. These adhesive forces produce localized deformation and in some systems transfer relatively undegraded or degraded polymers (i.e. chemical degradation due to temperature rise) to counter face. Therefore the extent and the rates of deformation are greater than those exist in the cohesive wear.

Chemical wear or corrosive wear is most certainly present in all wear processes. It ranges from mild chain scission to gross decomposition of polymer under intense loading. Unlike abrasion, fatigue or erosion, corrosive wear is associated with polymer surface and its interaction with the environment. This is an interactive cycle process. First, the exposed surface reacts with the environment and the products from the reaction are formed on the surface. Then, reaction products are wearing down as a result of abrasion caused by counterface or impact from the solid particles.

2.4 HARD COATINGS

Hard coatings are primarily used to resist wear in heavily loaded or at high temperature operating conditions. Coatings of ceramics, intermetallic alloys and cermets provide good wear resistance owing to their high hardness. However, most hard coatings are likely to expose to corrosive environments during their service life. The wear occurs on the coatings, which will likely expose the substrate beneath the coating and hence propagate the corrosion. Eventually the exposed substrate will break down due to degradation. Therefore it is essential to select the proper coatings based on their applications in related industries. The following section reviews several deposition techniques for hard coatings which range from conventional methods (e.g. welding overlay, CVD, PVD, thermal spraying) to newly emerging methods such as sol-gel and electrophoretic deposition.

2.4.1 Welding Overlay

All of the welding processes involve the melting of the coating material onto the substrates by gas flame, electric arc or plasma arc welding processes. When the coating

material solidifies, it welds the components together. The coating materials can come in the form of powder, paste, rod, strip or wire. Normally for weld deposition by arc, the substrate and the coating material must be electrically conductive. Thus most substrates and coating materials are in the form of metals or alloys (Bhushan and Gupta, 1991).

The weld deposits thickness can range from 750 μm to a few millimeters. Most weld deposition processes are capable of depositing on small components of intricate shape as well as large surfaces of flat or cylindrical shape. Furthermore, the welding equipment is also portable and relatively inexpensive. However, there are several inherent characteristics of weld deposition processes, which have to be considered. These include difficulty in controlling the deposition rates, the degree of penetration of the weld into the base metal, the inferior appearance of the deposited weld and metallurgical limitations imposed by the heat inputs.

Rapid heating cycles, high temperature and relatively rapid cooling rates to ambient temperature are responsible for the changes in microstructures developed across the welding zone. The high energy input during welding causes very different thermal effects than conventional heat treatment. A subsequent heat treatment is necessary in order to reduce residual stresses introduced after welding. These stresses may cause stress corrosion cracking (Easterling, 1983) which is deleterious to the coating.

The types of microstructure formed during the welding can be distinguished into several zones: weld metal, fusion line, coarse grained heat affected zone (HAZ), HAZ, fine-grained HAZ, intercritical HAZ and base material. The heat affected zone adjacent to the weld may become preferentially attacked in corrosive environment owing to the differences in composition or metallurgical changes during welding. Furthermore it is not easy to form an even, relatively thin and continuous coating by welding. The shape of the objects also limits the applicability of this method. Most importantly it is unlikely to deposit nanostructured coatings because there is no mechanism available now to inhibit grain growth of nanoparticles beyond the nano scale and control the metallurgical changes during welding.

2.4.2 Chemical Vapor Deposition (CVD)

Chemical vapor deposition (CVD) was introduced in 1950s. As implied in the name of the technique, it involves chemical reaction during the course of deposition. CVD process is an open system with a gas inlet and outlet line. This process involves gaseous reactants (precursors) which are activated thermally or by other means in a reaction chamber and then react to form a solid film (coating) on the substrate. Precursors can be in the form of gases, liquids or even solids at room temperature. The precursors not only react with the surface of the substrate and also on the walls inside the reactor. This method provides a wider deposition zone compared to physical vapor deposition and thus allowing the deposition of many substrates at the same time. Classification of CVD depends on the substrates temperature: high temperature CVD ($850^{\circ}\text{C} < T < 1200^{\circ}\text{C}$), moderate temperature CVD ($700^{\circ}\text{C} < T < 850^{\circ}\text{C}$), and low temperature CVD ($300^{\circ}\text{C} < T < 600^{\circ}\text{C}$) (Habig, 1986).

CVD reaction is controlled by thermodynamic equilibrium which in turn depends on the vapor pressure and temperature. Sequences of reactions involved in CVD process are as follows (Pierson, 1999):

- a) Diffusion of reactants to substrate surface through the boundary layer.
- b) Adsorption of reactants on the substrate surface.
- c) Surface events (e.g. nucleation, growth of critical nuclei, lattice incorporation and aging processes in the layer during deposition).
- d) Desorption of products from substrate surface.
- e) Diffusion of products from the substrate surface through the boundary layer.

The sequences are further illustrated in Figure 2-5.

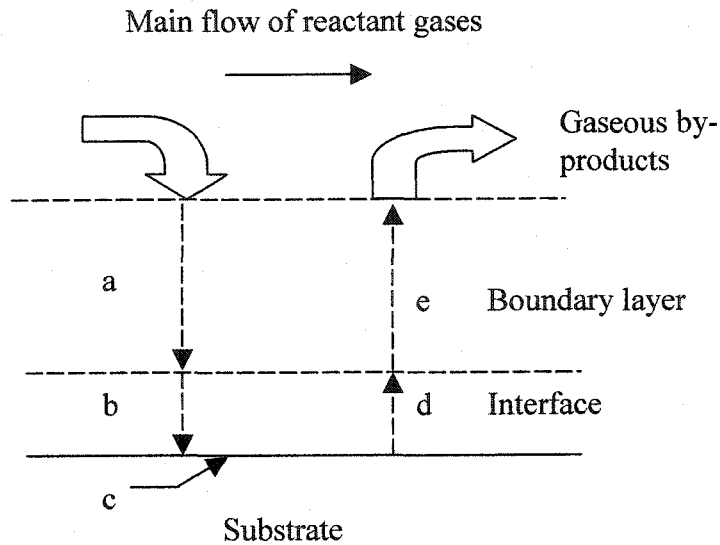


Figure 2-5 Sequence of events taking place inside the reaction chamber during CVD process (extracted from Pierson, 1999).

In a CVD coating process at “low” temperature, rate controlling steps are the surface processes. Therefore, the deposition rate, s (sec^{-1}) is given by Arrhenius law:

$$s = c \exp(-E/RT) \quad (2.5)$$

where $c = \text{constant}$ (sec^{-1})

$E = \text{activation energy}$ (kJ mol^{-1})

$R = \text{gas constant}$ ($8.314 \times 10^{-3} \text{ kJ mol}^{-1}\text{K}^{-1}$)

$T = \text{deposition temperature}$ (K)

At “high” temperature, the deposition rates are controlled by diffusion, which is temperature dependent.

$$s \propto T^{1.5} \text{ to } T^{2.0} \quad (2.6)$$

Two most commonly used reactors for CVD are hot-wall and cold-wall reactors. For the hot-wall reactor, the substrates as well as the tubes along the reactor are heated up to the deposition temperature. In this case, films deposit on both the substrates and any exposed area inside the reactor. Such predicament can induce possible contamination in the hot-wall reactor due to the interaction between the vapor and the inside walls of the reactor. Therefore, hot-wall reactors are ideal for exothermic reactions.

In contrast to hot-wall reactors, cold-wall reactors happen to promote heating on the substrates but suppress the rise of the temperature on the reactor walls. Therefore, reactions happened most readily at the heated surface since there is an existing temperature gradient between the substrates and reactor walls. Consequently, use of cold-wall reactors may greatly reduce the contamination inside the reactors. Cold-wall reactors are suitable for endothermic reactions.

2.4.3 Physical Vapor Deposition (PVD)

Physical vapor deposition or PVD was developed in 1852 by Faraday. It is the oldest and widely used method for thin film deposition. In contrast to CVD, PVD involves the condensation of material vapor generated by evaporation, sputtering, or ion plating onto a substrate to form a film with or without chemical reaction (Wahl et al., 2002). PVD encompasses a wider range of process combination than CVD. In order to prevent accumulation of residual stresses in the coatings, the film thickness seldom exceeds a few microns in PVD. PVD coatings are commonly used in gas turbine industries where the turbine blades are coated to prolong their service life. In tool making applications, TiN coatings by PVD are deposited onto high speed cutting tools in order to improve their wear resistance.

One of the oldest PVD techniques is by evaporation process. It is most commonly used because it is simpler and cheaper as compared to other vacuum deposition processes. During the process, the coating material (source) is heated to above its melting point so that it becomes vaporized in a vacuum chamber. The vacuum chamber typically operates between 10^{-3} and 10^{-8} Pa. The vaporized material or evaporated atoms travel from the source to the substrate through a path of line-of-sight due to the existence of the temperature gradients between the substrate and the source. Finally, the evaporated atoms will condense on all the exposed surfaces, including the substrate to be coated.

Other specialized evaporation techniques include flash evaporation, laser or electron beam ablation, cathodic arc evaporation (including filtered arc), and anodic arc evaporation. Most of these specialized techniques incorporate plasma into their systems. The plasma is used to enhance the reaction between the reactants (especially in reactive evaporation) or to cause ionization of the gas atoms in the vapor phase. Compared to the

sputtering process, the evaporation process usually results in a poorer adhesion between the coating material and the substrate.

Unlike evaporation, sputtering involves the momentum transfer of high kinetic energy ions that strike the surface of the source, resulting in the dislodge of the atoms from the source surface. The ejected atoms from the source travel at a very high velocity towards the substrate and bombard the surface of the substrate to result in the formation of a thin layer on the substrate surface. Typically, the high energy ions are created by an ion gun. Argon is widely used as the working gas because it is inert. The ion gun creates Ar^+ ions, imparts kinetic energy to the ions and directs the ions toward the target to be sputtered. The sputtering process operates in vacuum condition at around 10^{-2} - 10^{-5} Pa.

Ion plating is a hybrid of PVD process where the substrate is subjected to a high negative potential. The evaporated atoms pass through the glow-discharge region on their way to the substrate and become ionized in this region. The discharge potential is maintained as high as possible so that the ionized atoms are accelerated toward the substrate. Before deposition takes place, the substrate is constantly bombarded by the admitted Ar^+ ions for a sufficient time to remove surface contaminants. When the substrate surface is sputter-cleaned, the deposition process begins without obstructing the ion bombardment. The capability of sputter-etching process during deposition is effective in ensuring better coating adherence because the substrate is constantly cleaned (sputter-etched) from impurities. However, this means that some of the deposits will be sputtered away as well. Since both deposition and etching processes occur simultaneously, the deposition rate has to be higher than sputter-etching rate in order for the coating to form (Bunshah, 1994).

2.4.4 Thermal Spray

Thermal spraying is defined as a process where the coating material is fed to a heating zone where it is totally melted and then is projected to the pretreated substrate. The molten particles flatten as they strike the substrate, resulting in layers of coatings on the surface. The substrate is usually heated below 150°C , so that its metallurgical properties (strength, hardness etc) are unaffected. Any materials that can be melted without decomposition can be used to form the coatings. Two most common thermal

spraying processes are plasma spray and flame spray. Plasma spray includes atmospheric plasma spray (APS), vacuum plasma spray (VPS) and inert plasma spray. Flame spray process consists of a detonation gun (D-Gun) process and a high-velocity oxy-fuel (HVOF) process.

With reference to the sprayed materials, plasma spray is the most flexible thermal spray process. The energy source for plasma spray is an electric arc that is initiated with a high frequency discharge. Carrier gas such as Ar, He, or N₂ is fed into the arc. Once the gas passes the arc, reactions occur between the electrons from the cathodic source and the gas molecules, resulting in a dissociation or ionization of the gas (plasma state). The particles are injected into the plasma jet where they are melted rapidly. At the same time the molten particles are accelerated toward the substrate to be coated. The effective heat transferred to the particles depends on the enthalpy of the plasma, which in turn depends on the type of carrier gas.

Atmospheric plasma spray (APS) takes place in open air. Therefore, it is more suited for oxide powders because the sprayed particles can react with the oxygen in the atmosphere on their path from the plasma gun to the substrate.

To avoid the problem of particle oxidation in atmosphere, Inert Plasma Spray (IPS) process takes place in a chamber containing an inert atmosphere (usually filled with argon) either at or slightly above the atmospheric pressure. The inert gas prevents reactions of the plasma stream, the substrate, or the sprayed particles with the surrounding environment.

For a more stringent requirement with regards to the density, purity, and low oxide content of the coatings, another alternative is to use Vacuum Plasma Spray (VPS). VPS is implemented in an inert atmosphere chamber at a reduced pressure to prevent undesirable reactions of the plasma stream, sprayed material, and substrate with the surrounding atmosphere. Coatings are formed under higher energy state since the particles undergo less cooling or deceleration in the low-density gas. An article by Zhu et al.(2001), claimed that compared with other thermal spray methods, the coating of nanosized WC-Co onto a steel substrate through VPS exhibits higher hardness, toughness and wear resistance.

Flame spraying uses the thermal energy released from the oxygen-fuel flame to melt the feedstock materials. These feedstock materials are available in the form of powders or wires. Similarly, for the D-Gun process, the oxygen-fuel and coating material are introduced into the reaction chamber through inlet valves. The gas mixture is ignited by a spark plug, thus creating detonation heats and accelerates the powder to supersonic velocity down the reaction chamber. The coating material can accelerate up to 900 m/s when it hits the substrate. At the end of each cycle, argon or nitrogen is used to flush the chamber. This process is repeated many times a second. High-velocity oxy-fuel or HVOF process is most widely used for the production of tungsten carbide-cobalt group of coatings. For HVOF process, a high pressure is applied in the combustion chamber to result in an enormous increase in the velocity of the spraying particles. The flame travels through an extended passage from the reaction chamber and leave the nozzle of the spray gun at supersonic velocity (up to 2100 m/s) whereas the particle velocities could exceed 650 m/s (Kunst et al., 2002). The long passage ensures sufficient time for heating and acceleration of solid particles. The morphology and porosity of particles and flame characteristics determine the temperature and velocity of the particles in the jet, and thereby the amount of decarburization, the porosity, and the cohesion of the coating. Among the available thermal spray methods, this process produces much denser coatings with much better adhesion to the substrate as well as lower surface roughness and less cracking (Crawmer, 2001).

2.4.5 Electrochemical Deposition

Electrochemical deposition (also known as electrolytic deposition, electrodeposition or electroplating) involves deposition of metal ions which deposit on the cathode by the passage of an electrical current through an electrolytic bath. This process produces chemical bonding between the deposited material and the substrate, which is stronger than any mechanical bonding produced by thermal spray. The method does not require expensive materials or equipment and is feasible to components of any geometrical configuration. Moreover, the choice of coating and substrate may encompass a huge number of pure metals or alloys. Electrochemical deposition is closely related to

electrophoretic deposition except that the former primarily deal with ions whereas EPD concerns with the deposition of colloidal particles (Bunshah, 2001).

2.4.6 Sol-Gel

Science of sol-gel has undergone a major revolution over the last twenty years. Most early studies mainly centered on silica and silicate glasses and gradually extended to many ceramics and ceramic composites. The term sol is defined as a dispersion of colloidal particles of one phase in a fluid medium (i.e. water or organic liquid) and the gel is the gelatin that formed after aging (Massimo, 1997; Uhlmann et al., 1997; Zarzycki, 1997). This process involves four crucial steps: preparation of the precursor, application of the sol to a surface, evaporation of the solvent from the sol to form a gel and finally curing the sample. The methods of sol-gel deposition are primarily through spin- and dip-coatings.

Once the sol is applied on the substrate, the coated substrate is dried and fired, typically at 850°C for a short period of time. For more extensive densification and wear resistance, sintering temperature may need to be higher over a longer period of time. Dense ceramic materials like ceria, zirconia, titania and alumina have been produced and are used for improving corrosion and wear resistance.

2.4.7 Electrophoretic Deposition (EPD)

Electrophoretic deposition (EPD) is similar to the electrodeposition process except it is primarily concerned with the deposition of colloidal particles rather than ions. EPD consists of two steps, which are electrophoresis and deposition (Sarkar et al., 1997). Electrophoresis is the movement of the charged particles in a stable colloidal suspension towards the substrate under the influence of applied electric field. Then the particles are deposited on the substrate, which is known as deposition, see Figure 2-6. The advantage of EPD is its ability to coat on any hard-to-reach surfaces with uniform thickness (Boccaccini et al, 1998; Streckert et al., 1997)

The occurrence of electrophoresis was first discovered in 1807 by Reuss, who observed that charged particles suspended in a clay-water system migrate toward specific

direction when an electric field is applied across the suspension. However, it was not until the 1940s that people began to use electrophoretic deposition as a method to deposit coatings. After several refinements in the past decades, electrophoretic deposition now has been recognize as a flexible, simple and low-cost coating method. In fact, electrophoretic deposition can be applied to any solid particles that are available in fine powder forms so long as they can be dispersed easily in the suspension. Almost any class of materials including metals, polymer, carbides, oxides, and nitride can be deposited via EPD. In addition to being a coating method, EPD is also used for shaping monolithic, laminated and graded free-standing objects, and for infiltration of porous materials.

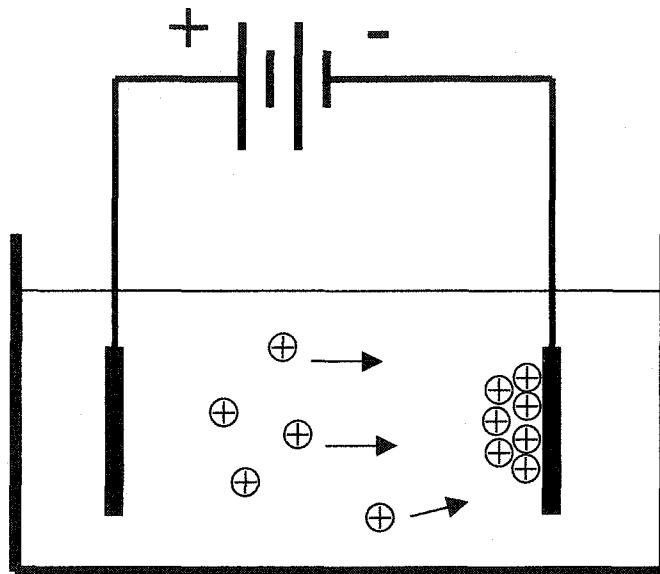


Figure 2-6 Schematic of an electrophoretic deposition process. Positively charged particles migrate to the negatively charged electrode (Randall and Tassel, 2001).

The deposition rate depends on the applied electric field, suspension concentration, and electrophoretic mobility of particles (Sarkar et al, 1997; Cabot and Foissy, 1998; Biest and Vandeperre, 1999; Windes et al., 2002). Fast deposition can be achieved in the order of seconds to minutes with a broad range of thicknesses from less than 1 μm to 45 μm (Belaroui et al., 2002). Selection of particle size to be deposited by electrophoretic deposition is also important because the particles must be fine enough to remain well-dispersed in the suspension during the coating process. Another important parameter that

should be taken into consideration is the medium used to suspend the particles during the EPD. Most of the published articles used organic-based instead of water-based suspension because the later causes a number of problems in electrophoretic process. Water-based suspension induces electrolysis at the electrodes even at low potential. It also has higher heat capacity than organic medium, leading to heating of the suspension and hence destabilizing the suspension. Despite the disadvantages of water-based EPD, there are several publications reporting successful EPD from water suspensions (Simovic et al., 2002). The reason is that water remains the most inexpensive and harmless resource than the organic solvents. Others demonstrated that using palladium as electrodes can eliminate the formation of gas bubbles. However, palladium is an expensive noble metal and its applications are very limited in industry.

Compared to water the dissociating power of organic medium is lower. Therefore an added electrolyte may only dissociate partially in the organic suspensions. This means that fewer ions are generated in the organic suspension. Under such condition, the particles may not be effectively charged as opposed to the charged in water of the same electrolyte concentration. Such drawback in creating high charges on particle surface can be overcome by applying higher electric field strength since electrolysis is unlikely to occur in organic solvents. Among all the organic solvents, the charging mechanisms of particles in alcohols are similar to water since both are amphiprotic solvents. The surface chemistry does not deviate drastically in alcohols since the hydrogen ion concentration continues to be a measure of the acidity of the medium.

During the EPD process, it is crucial that the particles must be colloiddally stable and well-dispersed in suspension. The particles, either sub-micron or nanometer in size should move independently with respect to one another in the suspension. The Brownian motion of such particles will keep them from settling as long as a barrier exists to prevent the particles from coming together. Under this condition, electrophoretic deposition can be performed during the manageable time scales (Randall and Tassel, 2001).

To avoid particles coming together by Van der Waals forces, repulsive forces must be established to develop a stable suspension. Addition of metal ions such as AlCl_3 , $\text{Mg}(\text{NO}_3)_2$, and MgCl_2 which selectively adsorb onto the surface of particles will cause them to establish surface charges. Having a high surface charge is definitely a key

advantage to develop a successful suspension. Meanwhile, the ionic concentration should be kept low as the suspension stability decreases with increasing ionic strength.

For the determination of surface charge, zeta potential can be a good indicator. It measures the electric potential at the slipping plane of the electrical double layer. In an electrolyte solution a cloud of counter ions surrounded a charged particle in the suspension, forming so called electrical double layer. The ions cloud eventually diffuses into the bulk concentration. When the counter ions and the particles are under the influence of an electric field, they move in opposite directions. However, a fraction of the counter ions will move together with the particles due to the attraction between them. The partition between these split ions is known as slipping or shearing plane. Therefore, zeta potential measures the net charge enclosed the particles instead of the surface charge of the particles (Biest and Vandeperre, 1999).

2.5 NANOSIZE PARTICLES

As the nanotechnology is sweeping through from every aspect of applications, there are practically no unaffected fields. The new direction for the coating industry is to use nanoparticles as coating materials and at the same time to adopt more flexible and versatile coating methods such as painting and EPD.

Nanoparticles are entities with diameters in the range of 1-100 nm. This new field of nanoparticles is lying between the traditional fields of chemistry and solid-state physics. Therefore, a significant gap exists between these regimes with unique characteristics that neither obeys the law of physics nor quantum chemistry. The smaller, the particle, the higher, the surface-to-volume ratio. Thus more atoms tend to reside on the surface than inside the particle itself. Particle chemical/mechanical properties that are once determined by the molecular structures are now influenced by the 'defects' of the exposed surface (Klabunde, 1996).

In other words, nanoparticles or nanostructured particles often display physical, chemical and biological properties that are remarkably different from coarse size particles. It has been demonstrated that nanosize particles exhibit a host of unique physical and chemical properties such as magnetic properties, optical properties, melting

point, specific heat and surface reactivity. Indeed, when nanoparticles are consolidated, they tend to display new and better mechanical properties (e.g. superplasticity and hardness) than their counterparts. These improvements in mechanical properties are anticipated in promoting the quality in coatings.

Besides the particle size, the grain size and geometry also determine dislocation movement and grain boundary sliding of nanoparticles to some extent. This in turn dictates the strength, hardness, ductility and toughness of these nanoparticles. When the structure scale (grain size) in a particle is reduced to the order of nanometers, the particle is known as nanostructured particle. Volume fraction of grain boundaries and triple junctions in a nanostructured particle increase tremendously as compared with conventional polycrystalline or amorphous counterparts (Wang, 2002).

2.5.1 Materials Selection

The most widely used material for cutting tools, e.g. drilling oil wells and in mining, is tungsten carbide. Tungsten is one of the most plentiful resources among the refractory material. Mixtures of tungsten carbide with binders such as cobalt or nickel will create a myriad of cemented tungsten carbide. The addition of binder improves the sinterability of tungsten carbide to fully dense material. However, the presence of binder reduces the hardness of tungsten carbide after sintering (Goren-Muginstein et al., 1998).

The hardness of the WC depends on the carbon content in its matrix as well. At the level of 94 to 97 weight percent carbon, a significant deterioration in the fracture toughness, strain tolerance and brittleness occurs. The choice of materials also depends on the coating methods, when electrolytic attack or etching of the binder exists, the choice of tungsten carbide in a nickel binder is preferable. Combination of tungsten carbide and nickel is more resistant than cobalt tungsten carbide to sodium hydroxide and hot sulfuric acid attack.

Another commonly used nano-size material is Al_2O_3 , which is far more readily available and cheaper than WC. Al_2O_3 has been known to exhibit high hardness, high melting point, and extreme chemical stability, which make it a suitable material for corrosion- and wear-resistant applications.

2.5.2 Yield Stress of Nanostructured Materials

In 1949, Hall found that the yield stress is dependent on the inverse square root of grain size. Petch also found the same dependence for the steel in liquid nitrogen. Later, both came out with an equation known as Hall-Petch (H-P) relation (Armstrong, 2001):

$$\sigma = \sigma_0 + \frac{k}{\sqrt{d}} \quad (2.7)$$

where σ = yield stress, σ_0 = friction stress, k = a constant and d = grain size.

This equation predicts the yield stress of coarse grain materials very well, but failed to predict the yield stress of nanostructured materials. Available evidence suggests that the Hall-Petch relationship should apply down to grain sizes at least as small as about 20-40 nm. Below that range, a reverse H-P behavior is likely to occur (Masumura et al., 1998; Koch, 2001).

2.5.3 Sintering Temperature of Nanosize Particles

Nanosize powders densify at a rate faster than their conventional counterparts, which eliminates the need for high temperature sintering (Livne et al., 1998). But such implication has its own upsides and downsides. The downside of high densification rate may lead to inhomogeneous heating of the nanoparticles where outer layers of the particles densify into a hard impervious shell which constrains the normal shrinkage in the core of particles. Due to the strain incompatibility, cracks can develop easily on the sintered nanoparticle surface. On the other hand, high densification rate may reduce the need to use additives. The sintering of conventional SiC serves as an example. Usually, boron or carbon additive is required for binding purposes. However, with ultrafine SiC, the densification takes place at a lower temperature without the addition of additives (Kijima, 1989).

2.5.4 Superplasticity

Most nanocrystalline ceramics exhibit a superplasticity behavior or the ability to withstand extensive tensile deformation without necking or fracture. The superplastic behavior is of industrial interest, as it can be used to produce objects of complex shapes.

The once brittle ceramics can now be superplastically deformed at modest temperature and then treated at high temperatures for strengthening. McFadden et al. (1999), observed that nanocrystalline ceramics/intermetallics deform at faster rates, lower stresses and lower temperatures. Nevertheless, at the test temperature where superplasticity deformation begins, the grain growth starts to show. As a result, the grain size becomes larger than the size of 100 nm or less desired commonly used for nanostructured materials. Furthermore, an article by Mayo (1997) indicates that superplasticity can easily disappear during deformation due to a combination of static and dynamic grain growth. In this case, a kinetic barrier is added to suppress the grain growth.

2.6 APPLICATION OF NANOSTRUCTURED PARTICLES

As discussed, PTFE (polytetrafluoroethylene) polymer has been a widely used engineering plastic because of its outstanding thermal stability, good resistance to solvents and low friction coefficient. One major shortcoming of PTFE is its high wear rate at normal friction condition and cold-flow phenomenon under load. Therefore, a lot of efforts have been devoted to reducing the wear of PTFE by inclusion of organic or inorganic particles (Li et al., 2002). Major improvement in mechanical properties of polymeric materials can be achieved by incorporating nanostructured particles into the polymer matrix.

In comparison with the conventional microscale particles, nanoparticles are believed to possess several advantages: (i) the angularity of particles decreases as their size decreases, therefore hard nanoparticles as fillers are preferable because they remarkably reduce the abrasive effect on the counterface (ii) the transferred film is strengthened because nanoparticles would also have the capability of blending well with wear particles; (iii) greater surface area-to-volume ratio is important for bonding nanoparticle to the polymer matrix in the composite material (Schwartz and Bahadur, 2000).

In 1996, Wang et al. studied the tribological behavior of polyetheretherketone (PEEK) filled with nanometer ZrO_2 . They found that nanometer ZrO_2 -filled PEEK composites can reduce the friction and wear of pure polymer. Based on their experimental results, the wear rate of the polymer composites was found to decrease gradually with decreasing particle sizes. In a subsequent study, Wang et al. (1997)

reported that PEEK filled with SiO₂ nanoparticles displayed lower wear rate and lower coefficient of friction. But, neither the studies provided reasons for the tribological effect.

Ng et al. (1999) used an ultrasonic device to disperse TiO₂ nanoparticles in epoxy. The resultant polymer nanocomposites appeared to be tougher than the traditional microparticle filled epoxy and also possessed a higher scratching resistance. Schwartz and Bahadur (2000) filled polyphenylene sulfide (PPS) with alumina nanoparticles. These samples showed good dispersion of filler particles in the PPS matrix under examination of SEM. Wear tests were performed on a four station pin-on-disk tribometer. Maximum wear resistance was found at weight percentages below 10. As the percentage of filler increased above this optimum, the composite material experienced more wear than the unfilled counterpart.

Recently, Wetzel et al., 2002 attempted to determine the optimum performance of polymer composites through the reinforcement of micro- and nanofillers. It is important to understand the role played by these inorganic fillers on micro- and nanometer scales so that of their wear mechanisms can be mapped.

CHAPTER 3 EXPERIMENTAL PROCEDURE

3.1 MATERIALS

3.1.1 Substrate

All the substrates used for Vickers Micro-hardness measurement, Universal MicroTribology Tester and erosion-corrosion tests is 1018 low carbon steel since it is widely used in industry. For Taber abrasion test, steel panels were purchased from Taber Industry. Each panel has a standard area of 100 mm square with a 6.3 mm diameter hole in the center.

3.1.2 Polymer

The polymer used in this study was obtained from Solomon Coatings, Edmonton, Alberta. It is commercially known as Xylan 1810 and consists of PTFE compound. Xylan 1810 is a thermoplastic polymer. The density of Xylan 1810 is 1.13 kg/m³. Another polymer was purchased from Madison Chemical Industries Inc. The product name is GemThane Precatalyzed Aromatic (GTPA) which is a single component aromatic polyurethane. GTPA is a thermoset polymer.

3.1.3 Powder

Nanostructured tungsten carbide (WC) particles of about 40 nm grain size were obtained from Inframat Corporation, USA. The Al₂O₃ powders (i.e. 50 nm and 300 nm) were obtained from Alfa Aesar. The original particles were cleaned prior to their use in order to remove any contaminant on the particles.

3.1.4 Silica sand particles

Silica sand particles were purchased from U.S. Silica Company of type AFS 50/70 (American Foundrymen's Society). The size of the particles is within the range of 200 to

300 μm . Other physical and chemical properties of the sand particles are tabulated in Table 3-1.

Table 3-1 A summary of the physical and chemical properties of the sand particles.

Property	Color	Hardness (Mohs)	Shape	Specific gravity	SiO ₂ Content (%)
Sand particles	White	7	Irregular	2.65	99.7

3.1.5 Chemicals

All the experiments were carried out in deionized water from a Millipore water purification system. Analytical grade NaCl was used to prepare the solutions for the corrosive and erosive tests. HCLP grade acetone from Sigma Aldrich was used as the organic solvent to wash the powders during centrifugation.

3.2 EXPERIMENTAL PROCEDURE

3.2.1 Preparation of Powders

About 5~10g of nanostructured WC particles were placed in a 50 ml centrifuge tube. Organic solvent (i.e. acetone) was poured into the tube up to 50 ml bench mark. The mixture was stirred with a spatula to expose the surface of WC particles to the organic solvent and then separated by centrifuge (IEC HN-SII Centrifuge) at a rotational speed of 3500 rpm for 5 minutes. After centrifugation, the heavy nanostructured WC particles settled at the bottom of the tube, resulting in a clear supernatant. The supernatant was decanted from the tube. To ensure the removal of the contaminants, the sediment was washed by deionized water for three times using the same procedures as used in washing by acetone. Finally, the sediments in the tube were dried in a vacuum oven below 80°C for several days. The Al₂O₃ particles were washed followed the same cleaning procedures as described above.

3.2.2 Preparation of Polymer Suspension

In this study, a number of nanoparticle-polymer suspensions was prepared. Table 3-2 summarizes the nanoparticles in polymer suspension used in this study. In preparation of nanoparticles-in-polymer suspension, the particles were blended in the Xylan 1810 solution at the solid to polymer mass ratio of 5:95, 10:90 and 20:80, resulting in suspensions of 5, 10 and 20 wt% particles, respectively. The weighed particles were first wetted with respective solvents specific for each polymer. For Xylan 1810, the particles were wetted by Solvent 100 which is a mixture of Xylene, N-methylpyrrolidone (NMP) and Methyl Ethyl Ketone (MEK). As for GemThane, particles were wetted by acetone. Then the polymer was added to the wetted particles to the desired amount.

Table 3-2 A summary of nanoparticles in polymer suspension used in this study.

Legend	Wt% of WC	Wt% of Al ₂ O ₃	
		50 nm	300 nm
Xylan 1810	0	0	-
	5	5	-
	10	10	10
	20	20	-
GemThane	-	0	-
	-	10	-

To ensure a good dispersion of the particles in the polymer solution, the mixture was ultra-sonicated before spin coating. The mixture was placed in an ice bath to prevent over-heating of the polymer-nanoparticle suspension during the sonication using an ultra-sonic dismembrator (Model 550, Fisher Scientific). The amplitude of the dismembrator was set at 50 % and the sonication time, for 10 minutes. To avoid sedimentation of the particles in polymer suspension, the spin coating was performed immediately after dispersion.

3.2.3 Spin Coating

Spin coating is an easy and common method for coating a thin, smooth layer of polymer on a flat surface. The thickness of the coatings is controlled by the viscosity and the centrifugal force that is parallel to the substrate. At a low rotation speed, the coating solution spreads out on the substrate. At a high rotation speed (generally 2,000 ~ 4,000 rpm), excess polymer spins off of the substrate and thin films are formed (Kim et al., 2002). This method is definitely a simple and more effective way of making thin film coatings as compared to the conventional physical and chemical methods. The film thickness is controlled by parameters such as the time and the speed of rotation as well as the viscosity and concentration of the coating solution. Despite these notable attractions, spin coating is not a versatile method to coat on objects of irregular shape. In fact, spin coating is more suitable for laboratory scale usage. At a larger scale, the coating solution is best applied by a spray gun.

In our study a 1018 carbon steel disk with a surface area of 7.09 cm² and thickness of 2 mm was used. First, the sample was placed onto the spin chuck. Vacuum line was turned on to hold the sample in place. Using a disposable pipette, a given volume of polymer suspension was dispensed on to the substrate to cover ~ 100% of the surface area of the substrate. After dropping the coating suspension onto the substrate, spinning of the substrate was started. The spin coating method is illustrated in Figure 3-1.

To completely seal the substrate, a thin layer of pure polymer was first spin-coated at 2000 rpm for about 30 sec. After this, the samples were baked in an oven (Lindberg/Blue Model 51731) at 360°C for 20 minutes. When the first layer was set, a second layer of nanoparticle-polymer suspension was deposited on the substrate by the same procedures. After coating the second layer of nanoparticles-polymer layer, the sample was baked again under the same condition as for the first coated layer. Figure 3-2 depicts the two layers of coating deposited on the substrate.

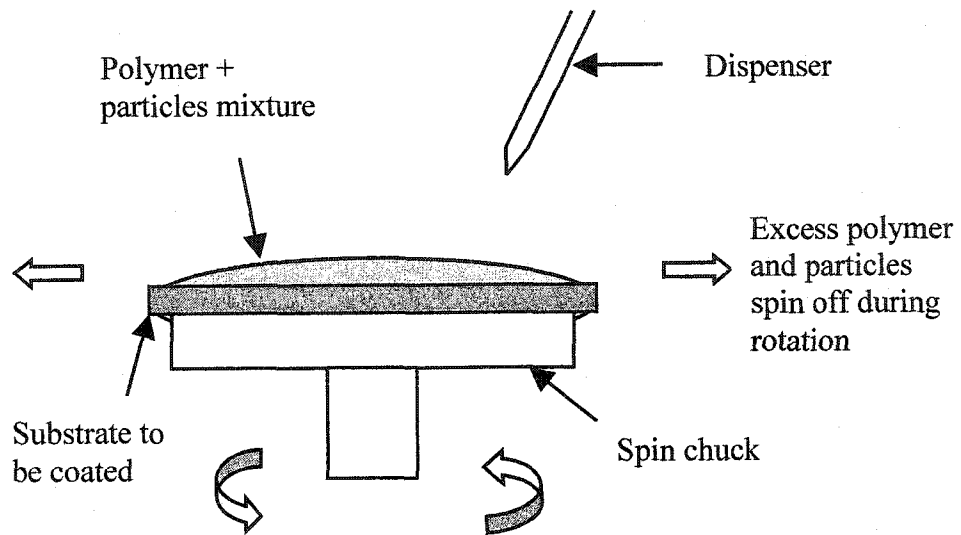


Figure 3-1 Illustration of spin coating method. Excess suspension spins off during rotation, leaving a uniformly distributed coating.

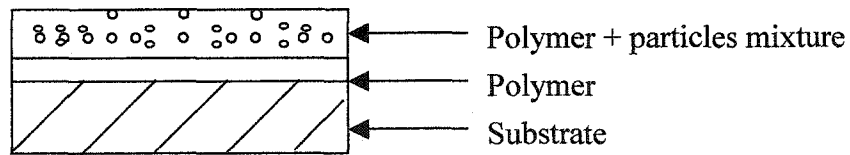


Figure 3-2 Schematics of coating layers on a substrate.

3.2.4 Taber Abrasion Test

Coatings, under the preparation conditions listed in Table 3-2, were prepared to a thickness of 10 mils (i.e. 254 μm). The particle-polymer suspension was spread on the panel using a hand-held applicator blade (ASTM D 823-95). The coating film with uniform thickness was cured on the panel.

3.2.5 Vickers Microhardness Tester

To evaluate the role of nanoparticles in enhancing mechanical properties of the coated polymer composite layers, the Vickers microhardness were measured on a Shimadzu Microhardness Tester apparatus which is connected to a data processor. A pointed diamond pyramid with a square base is used as the indenter. The principle of hardness measurement is straightforward. The indenter is pressed against a work /test piece at a pre-selected load. The average diagonal length (D) of the resulting impression on the test piece is measured by adjusting the left and right scale lines with the aid of a mounted optical microscope head, as shown in Figure 3-3.

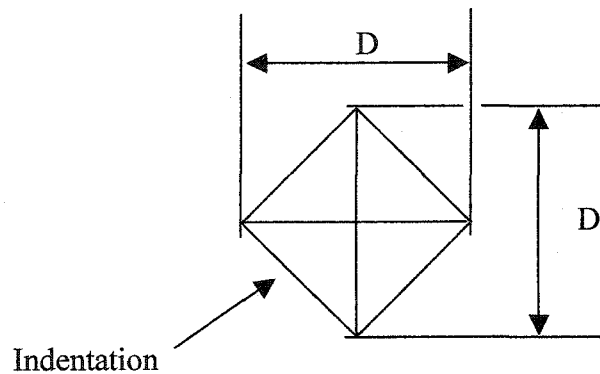


Figure 3-3 Schematics of a typical indent.

Vickers microhardness number (HV) is computed using the equation as shown below:

$$HV = 1854.4 P/D^2 \quad (3.1)$$

where P = test load (g)

D = length of diagonal line of indentation (μm).

In this study, the hardness tests were performed under the applied load of 50 g and the loading time was 15 seconds for all the samples.

3.2.6 Universal MicroTriboscope Tester

The scratch tests were performed on a Universal MicroTriboscope (UMT) that is equipped with a mounted tungsten carbide tip. The movement of the tip is monitored through a computer. The shape of the indenter is shown in Figure 3-4. The principle of the technique is to impose a well-defined force on the indenter into a smooth surface which moves perpendicularly to the indenter's motion, see Figure 3-5.

At the beginning of each experiment, the tungsten carbide indenter was fixed to the indenter holder. The specimen was positioned firmly on a platform to provide rigidity in the x-y plane. Prior to the test, the indenter was moved as closely as possible to the specimen surface. The velocity of tip movement was set to be 0.02 mm s^{-1} . Both vertical and horizontal forces were captured by the piezoelectric force transducer and the data, stored by the computer. Two different types of tests were performed on all the samples, one under a constant load of 20g and the other under progressive load from 0 to 25g. Morphologies of the scratches were examined with an optical microscope and SEM. Because the polymer composite film is non-conductive, the samples for SEM were coated with a thin layer of gold (20 to 30 nm) by sputtering method.

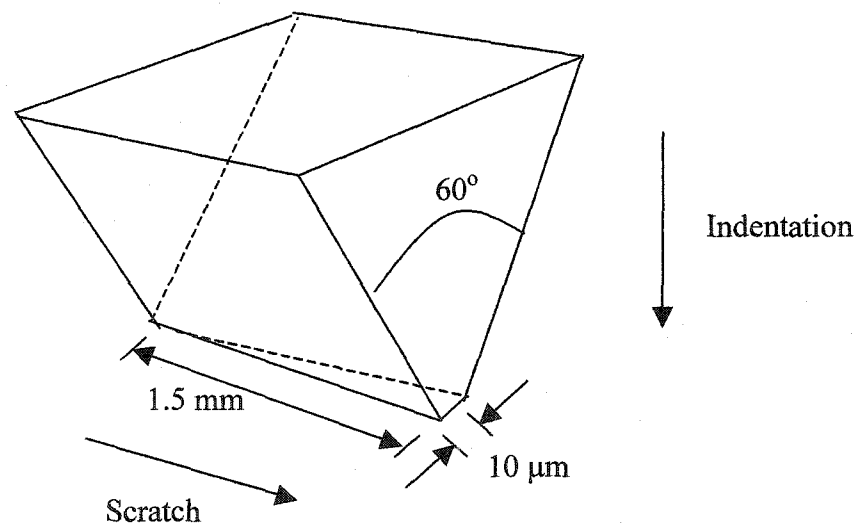


Figure 3-4 The geometry of the probe for scratch tests.

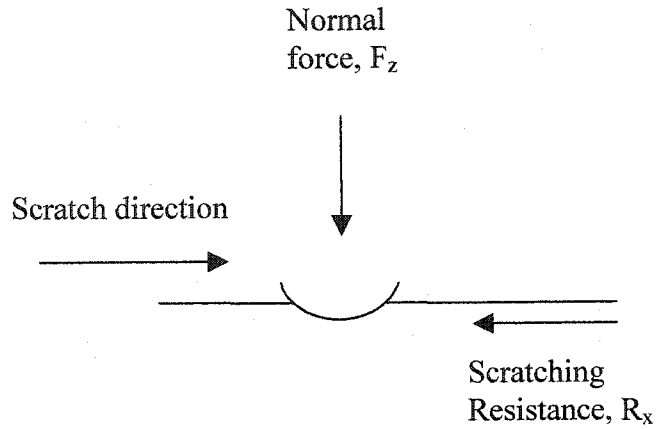


Figure 3-5 Basic principle of scratch test.

3.2.7 Abrasion Resistance

Taber Abrasion Tester used in this study is a model 5130. The abrading wheel used was Calibrade H-10, which is a non-resilient wheel composed of vitrified clay and silicon carbide particles. Cured sample is mounted to a rotating turntable and subjected to wearing actions of two abrasive wheels with a weight load of 500g on each side, see Figure 3-6.



Figure 3-6 Taber Abrasion Tester—Abraser Model 5130

The testing procedures were carried out in accordance with ASTM D 4060-95 with the exception of the abrading wheels. For each coating, test was repeated three times and average value was reported. The abrasion resistance or wear rate of coatings is expressed as the volume loss per number of revolutions. All abrasion tests were performed in a dry condition for 200 cycles.

3.2.8 Electrochemical Method – Potentiodynamic Polarization Scan

DC polarization method such as potentiodynamic polarization is often used for laboratory corrosion test with the DC polarization technique, useful information regarding the corrosion mechanisms, corrosion rate and corrosion susceptibility of coatings in a designated environment can be obtained. The potentiodynamic polarization involves varying the potential of the working electrode at a selected scan rate and monitoring the current response. In a potentiodynamic experiment, the driving force (i.e. the potential) for anodic or cathodic reaction is controlled, and the reaction rate (i.e. current) is observed. Typically, the current is expressed in terms of the current per unit area of the working electrode, i.e., the current density.

One of the pieces of information is often retrieved from the potentiodynamic polarization scan is the corrosion current density, i_{corr} . The corrosion current density is expressed by Tafel equation, as follows;

$$\eta = \pm \beta \log (i/ i_{\text{corr}}) \quad (3.2)$$

where $\eta = E_{\text{applied}} - E_{\text{corr}}$ (mV)

β = Tafel slope (mV)

i = measured current density (A/cm^2)

The i_{corr} at an open circuit potential is determined from the Tafel slope of the polarization curve, as illustrated in Figure 3-7. Once these slopes have been established at the linear regions of anodic and cathodic reactions, it is possible to extrapolate from both the anodic and cathodic regions back to corrosion potential, E_{corr} . The current density at

that point is defined as the corrosion current density (i_{corr}). The i_{corr} is related to corrosion rate, therefore, larger value of i_{corr} means higher corrosion rate and vice versa.

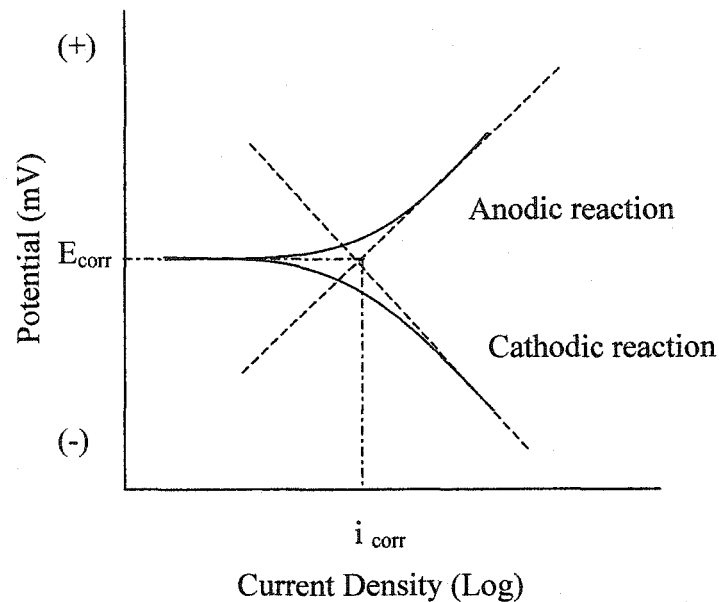


Figure 3-7 Extrapolated polarization curves for anode and cathode reactions to obtain i_{corr} values.

The potentiodynamic study was carried out in a typical three-electrode arrangement with the coated sample as a working electrode, a platinum coil as the counter electrode and a standard calomel electrode (SCE) as the reference electrode. A wire was soldered to the working electrode on the opposite side of the coated surface. The corrosion behavior of the coated and uncoated 1018 low carbon steel (7.09 cm^2) is studied in a 3 wt% sodium chloride solution at room temperature by using a computer-assisted potentiostat (EG&G PAR 273). Potentiodynamic polarization measurements were conducted by sweeping the potential from -0.25 to 0.25 V vs open circuit potential (OCP) at a 1.66 mV/sec scan rate. The surface morphology of the coated and uncoated samples was examined before and after tests by an optical microscope. During the experiments, sides of specimens except for the area of interest were sealed with an epoxy to minimize experimental errors. In order to minimize the ohmic drop of the solution, the capillary tip was positioned within 3 mm of the electrode surface. The potentiodynamic measurements

were taken at the beginning of the test and at different time intervals, finishing after 24 hours. Throughout the course of the measurement, the samples were always immersed in the solution.

3.2.9 Erosion-Corrosion (E-C) Test

Figure 3-8 shows a schematic representation of the experimental device constructed in this study for erosion-corrosion test. A series of tests were conducted on the coated and uncoated specimens. Four specimens were mounted to each substrate holders to increase the confident level for the weight loss measurement. A detail illustration of the E-C cell is shown in Figures 3-9, 3-10 and 3-11.

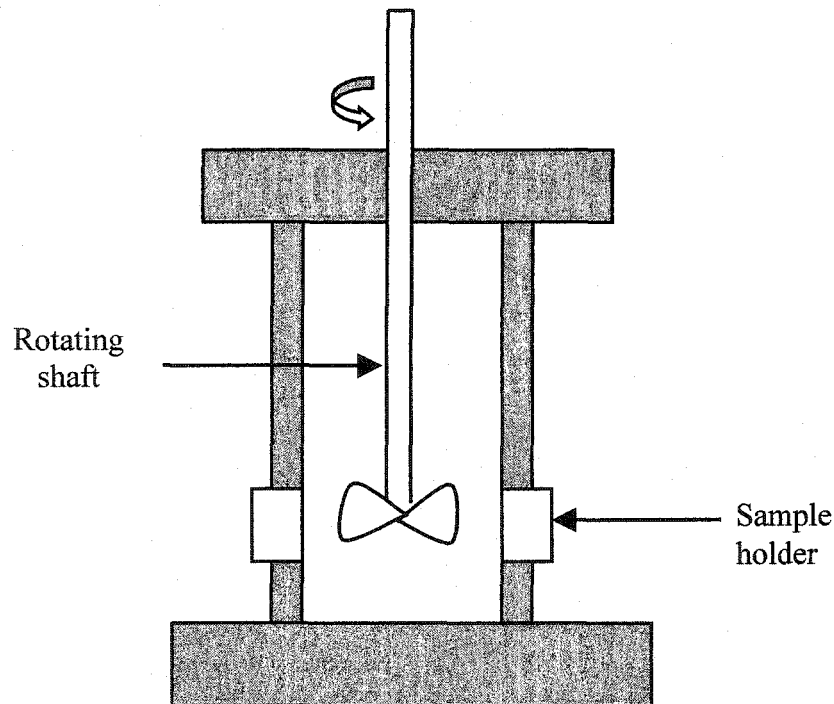


Figure 3-8 Experiment setup for the erosion-corrosion test.

The E-C cell was designed in such a way that it is high enough to prevent water from flowing out on top of the cell due to the high rotational speed of the shaft. A cover with a

center hole of 1.0 cm is designed to cover the top of the cell to minimize water from spilling. The purpose of the center hole is to place the shaft at a consistent spot during every E-C test. The base of the cell was attached to a heavy piece of metal in order to keep the cell stable during E-C test.

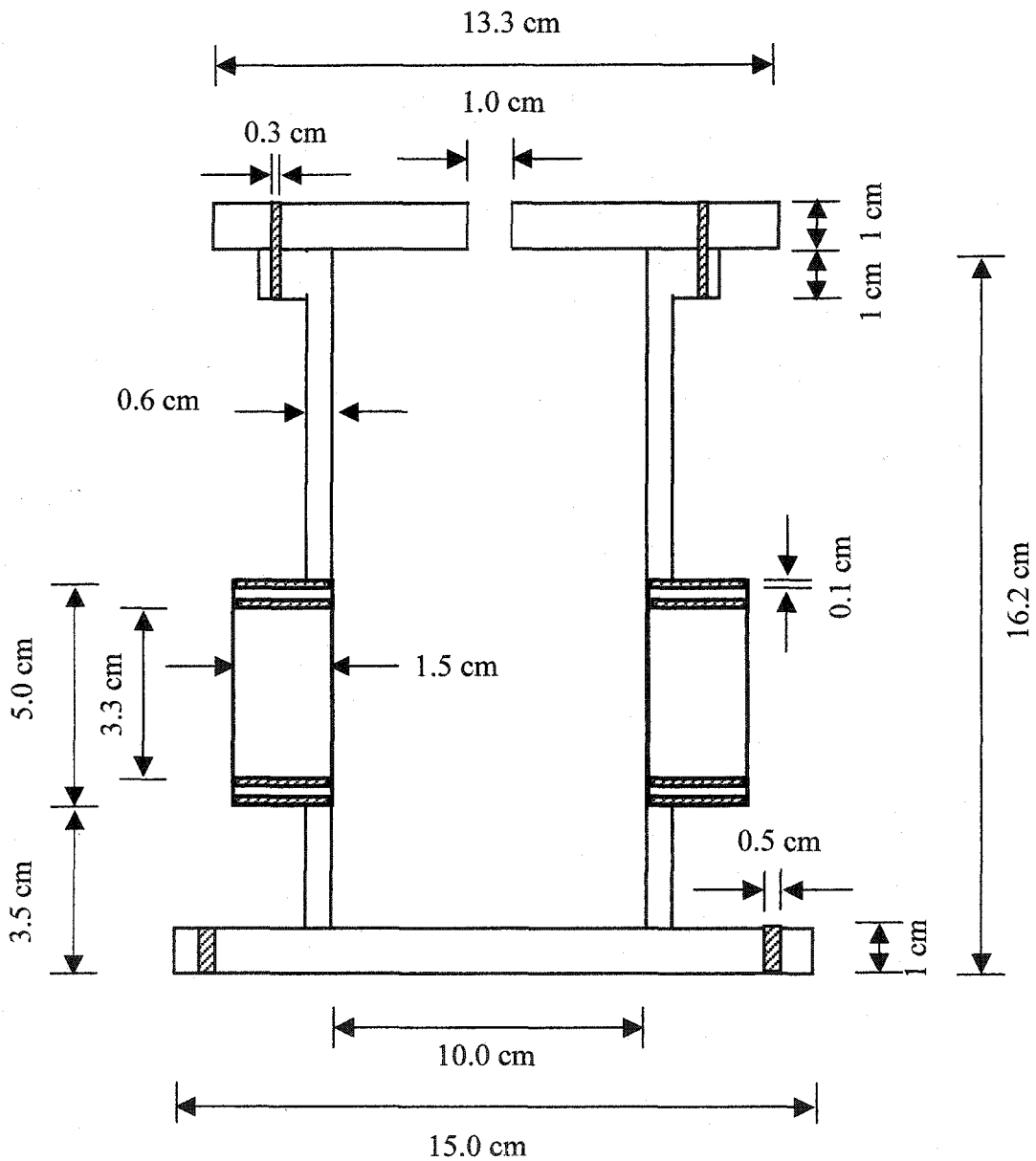


Figure 3-9 Details dimensions of the E-C cell (Side view).

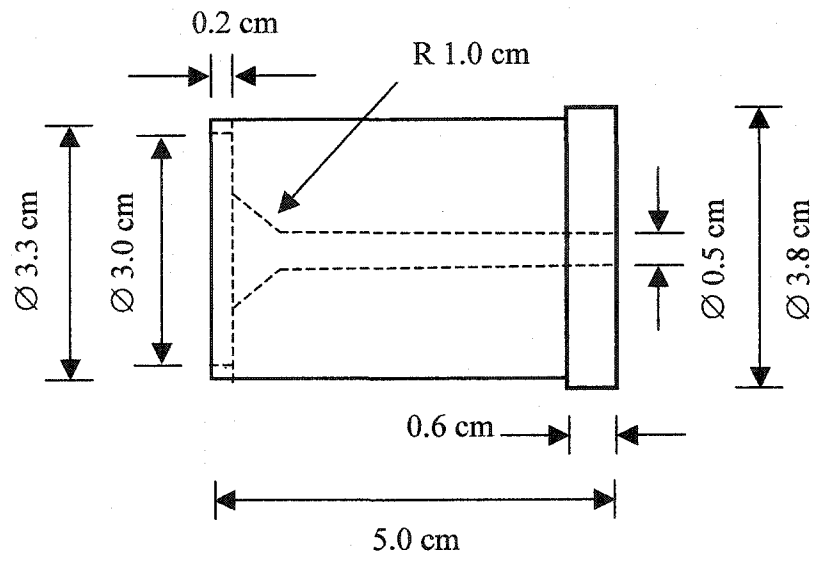


Figure 3-10 Details dimensions of the sample holder used in E-C test.

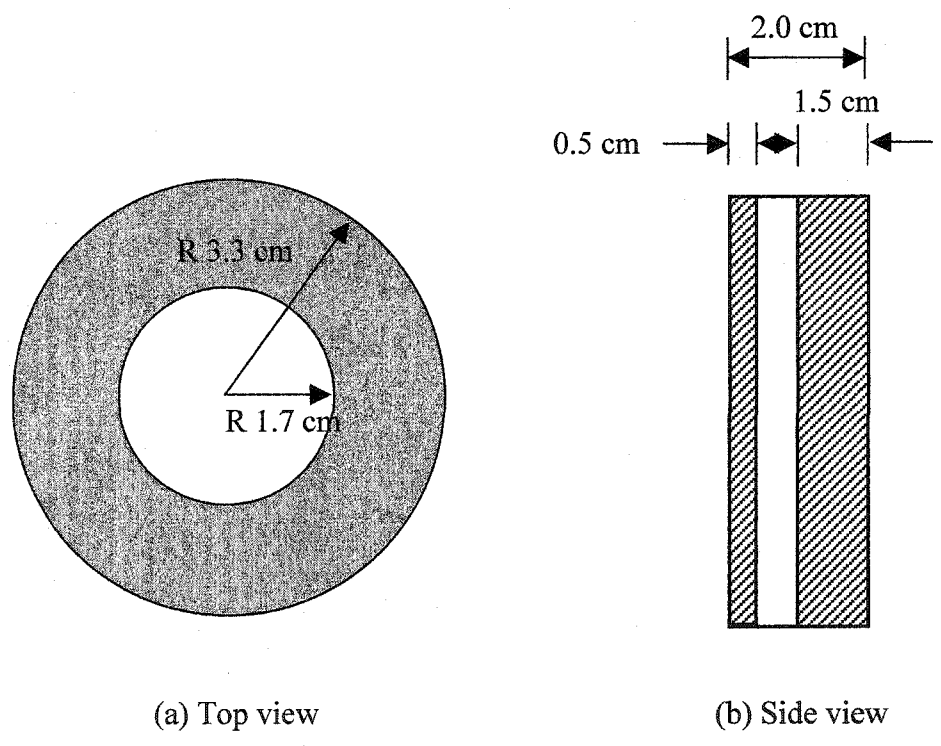


Figure 3-11 Plastic cover is used to seal the O-ring and sample holder together to prevent leakage as well as to keep the sample holder stationary during E-C test.

The sample holders, as shown in Figure 3-10, were designed to fit in perfectly into the E-C cell. A plastic cover (see Figure 3-11) was used to tighten O-ring and sample holder together in order to avoid water from leaking out from the cell as well as to keep the holder stationary during E-C test. The test sample was glued to the front side of the sample holder of 3 cm in diameter using silicon and was left overnight in order for the silicon to become hardened. The edge of the substrate was shielded from exposing to the test environment by extending about 0.2 cm of the circumference of the sample holder.

Silica sands used as the erosive component in this test was shown in Figure 3-12. For the E-C experiment, the solution was the same as in the corrosion test with the addition of 20 wt% sand. The rotating shaft was connected to Stir Pak mixer (from Fisher Scientific) and rotating at 1590 rpm throughout the tests. At the end of each test, the specimens were rinsed with water, blow-dried with air and weighed. The weight loss was measured every 6 hours until the coating shows visual degradation. The morphologies of the wear traces were observed under the optical microscope before and after the tests.

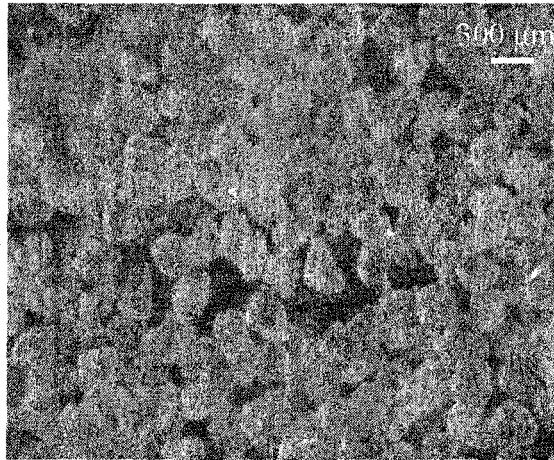


Figure 3-12 Irregular shape of sand particle used for E-C test is approximately 300 μm in size.

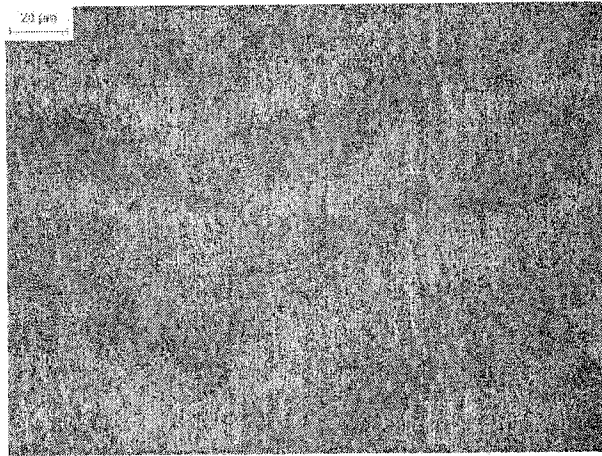
CHAPTER 4 RESULTS & DISCUSSION

4.1 MORPHOLOGY OF COATINGS

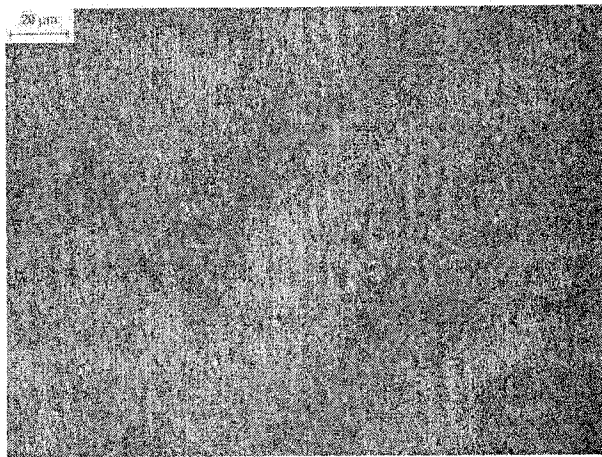
4.1.1 Coatings after Heat Treatment

Figure 4-1 depicts optical micrographs of polymer and its composite coatings. In Figure 4-1(a), the surface of polymer is seen as an even and smooth surface. Some lines observed on the surface could be due to the inherent property of the polymer itself or caused by the surface roughness of the substrate which may obstruct the polymer layer set perfectly during curing process. Figures 4-1(b), (c) and (d) show the morphology of polymer composite coatings containing 50 nm Al_2O_3 , 300 nm Al_2O_3 and 300 nm WC particles, respectively. The content of particles is fixed at 10 wt%.

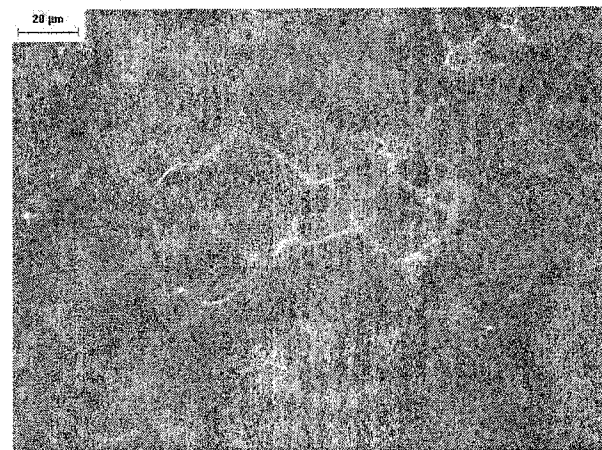
Figure 4-1(b) shows that 50 nm Al_2O_3 particles are uniformly distributed in the polymer matrix. No aggregates or clustered of Al_2O_3 particles are exposed on the coating surface. As shown in Figure 4-1(c), the composite coating containing ultra-fine (300nm) Al_2O_3 particles is not as uniform as the nanosize Al_2O_3 composite coating. The 300 nm Al_2O_3 particles formed clusters on coating surface. Similarly, the nanostructured WC particles are also poorly distributed in the polymer matrix as shown in Figure 4-1(d). The observed morphologies are strongly influenced by the dispersive state of the respective suspensions after ultrasonic treatment. The nanosize Al_2O_3 particles are more dispersive than ultra-fine Al_2O_3 and WC in the polymer solution as visually observed.



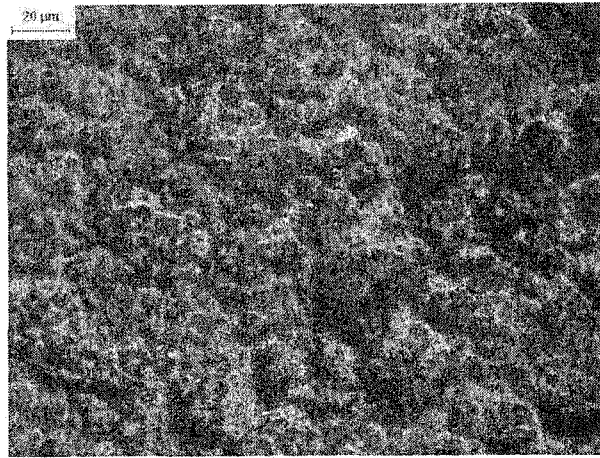
(a)



(b)



(c)



(d)

Figure 4-1 Optical micrograph of coatings: (a) polymer alone (b) 10 wt% 50 nm Al_2O_3 composite; (c) 10 wt% 300 nm Al_2O_3 composite; and (d) 10 wt% WC composite (dark area: WC clustered and light area: polymer).

4.1.2 Cross-section of Coated Sample

Figure 4-2 is an optical micrograph of the cross-section of a 10 wt% WC composite coating. The sample was polished using a 600 grits sand paper before it was examined under the optical microscope. The estimated total thickness of the two-layer coating is about 25-30 μm .

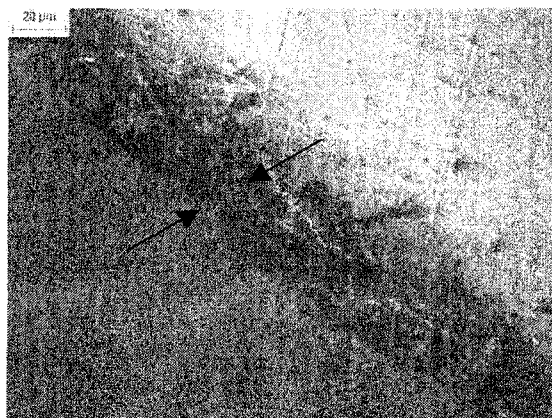


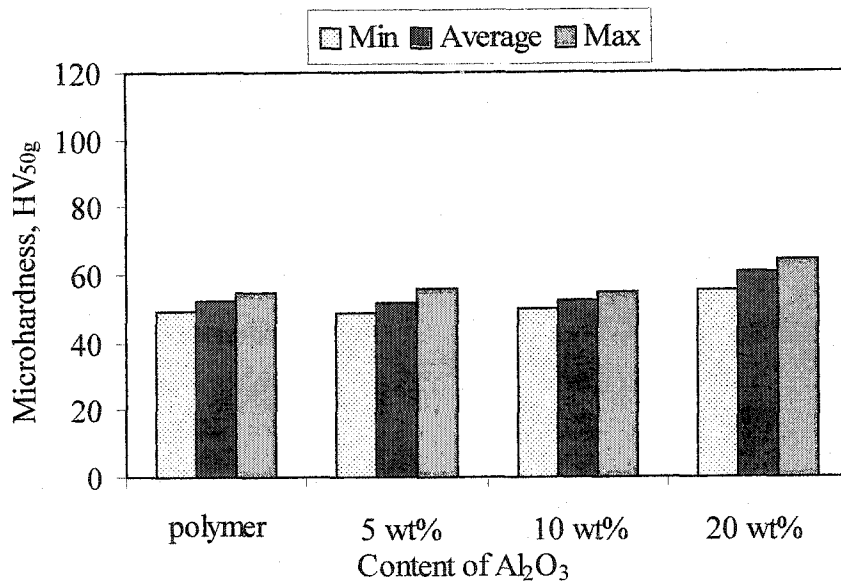
Figure 4-2 Cross-section of 10 wt% WC composite coating

4.2 MICROHARDNESS

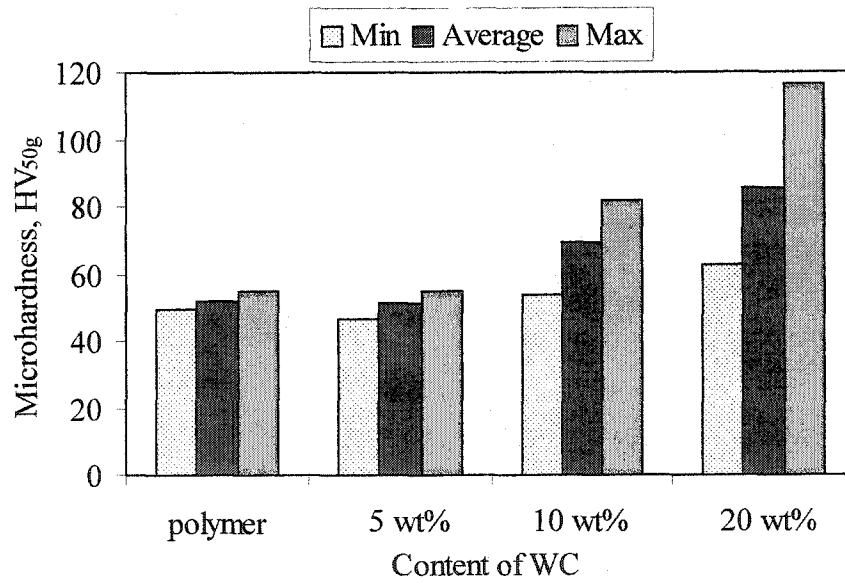
Microhardness measurement is one of the most reliable methods to determine microhardness of a test sample. The indent marked on the sample surface by an indenter at a pre-determined load is a measurement-stick of the microhardness of the sample. The diagonal lines and depth of an indentation are influenced by the applied normal load. Therefore, a small load (i.e. 5 g to 1000 g) is suitable for samples with thin coatings in order to minimize contact between the indenter and the substrate.

The Vickers microhardness test results for 50 nm Al_2O_3 composite coatings and WC composite coatings are shown in Figures 4-3(a) and (b) respectively. Figure 4-3(a) shows that the addition of Al_2O_3 to polymer coatings hardly improved the microhardness. The 5 and 10 wt% Al_2O_3 composite coatings displayed similar microhardness values of 52 $\text{HV}_{50\text{g}}$ as the polymer coatings. As Al_2O_3 content increases to 20 %, there is only a slight increase in the microhardness of Al_2O_3 composite coating. It is therefore safe to conclude from the indentation test that the Vickers microhardness of Al_2O_3 containing polymer composites does not change with Al_2O_3 particle contents.

For the case of nanostructured WC composite coatings, Figure 4-3(b) shows that Vickers microhardness increases steadily with increasing the content of nanostructured WC particles in polymer matrix. To improve the microhardness of WC polymer composites, a minimum of 10 wt% is required. Further increasing WC content to 20 wt% WC, the registered Vickers microhardness increased to 83 $\text{HV}_{50\text{g}}$. The difference between the recorded maximum and minimum microhardness values also increased with increasing the amount of nanostructured WC particles in the polymer composites.



(a) Microhardness of Al₂O₃ composite coatings.



(b) Microhardness of WC composite coatings.

Figure 4-3 Microhardness measurements for polymer and its composite coatings at applied constant load of 50g

Effect of Particle Size

A different range of sizes of Al_2O_3 particles were selected to determine the effect of particle size on the microhardness of the coatings. In this case, the amount of Al_2O_3 particles dispersed in the polymer matrix is fixed at 10 wt%. As seen from the bar chart in Figure 4-4, the microhardness of 50 nm Al_2O_3 is 52 HV_{50g} . As the particle size gets 10 times larger, microhardness of 300 nm Al_2O_3 composite coating is approximately 70 HV_{50g} . This microhardness value is about the same as 10 wt% WC composite coatings. Since particles of 300 nm Al_2O_3 and 10 wt% WC are highly agglomerated in polymer suspensions, it appears that the mechanical properties of particle-filled polymer coatings can be dramatically influenced by the degree of particles dispersion in polymer. The agglomerates in the composite coating surfaces may increase the hardness locally and then reduce microscopic deformation.

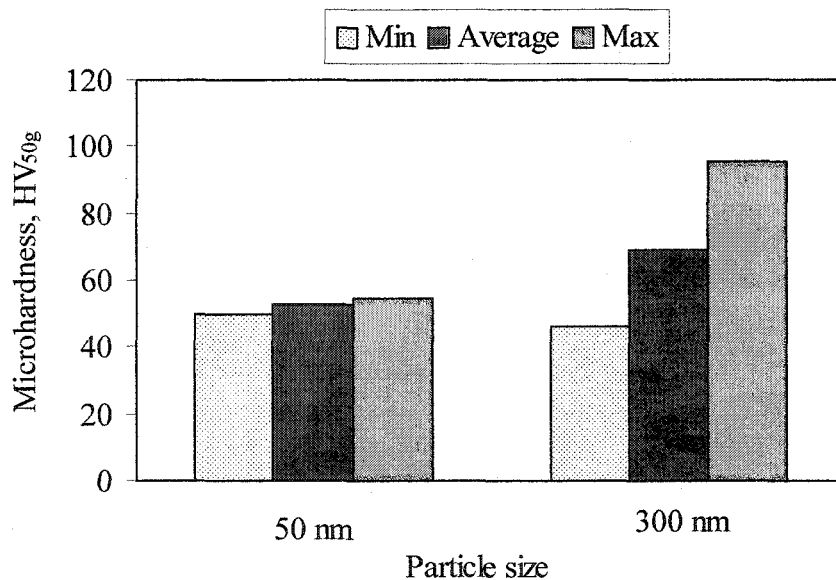


Figure 4-4 Effect of particle size on hardness of Al_2O_3 composite coatings.

Based on the indentation results, it appears that the embedded nanosize Al_2O_3 particles in polymer exhibits little in microhardness of Al_2O_3 composite coatings, whereas ultra-fine Al_2O_3 particles show a similar increase in microhardness value as 10 wt% WC composite coatings. The hardness of composite polymer is related to particle size, content

of particles and particle distribution in polymer matrix (morphology). In general, WC composite coatings exhibit a higher microhardness than nanosize Al_2O_3 composite coatings. But, as these particles (same particles size and content) were dispersed in polymer, the difference in microhardness between the two composites coatings is hard to distinguish.

4.3 SCRATCHING RESISTANCE

4.3.1 Scratching Resistance of Coatings

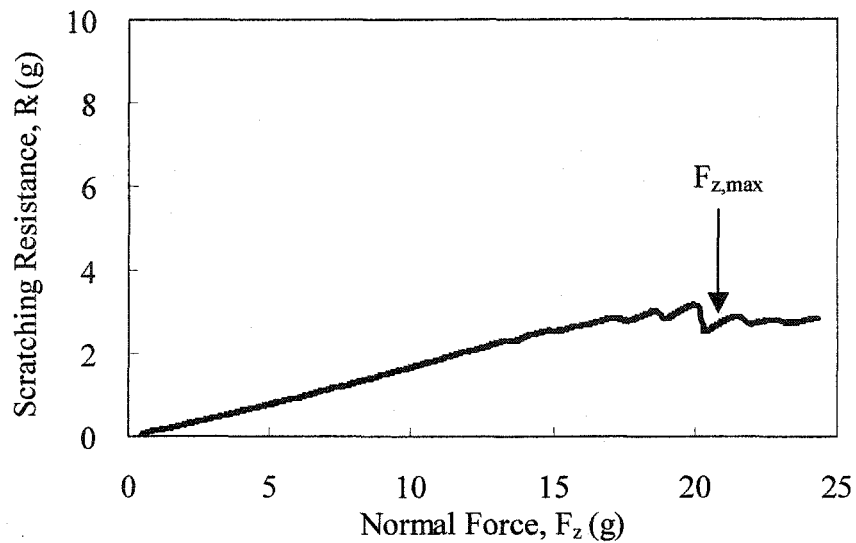
In general, scratching resistance, R_x , which reflects the resistance of a coating towards scratching, would increase linearly with increasing normal force, F_z , if there are no damage occurred during progressive loading. For this study, the objective of performing the progressive load scratch tests is to detect the onset of failure of the coatings. With the continual increase of normal force, scratch deformation changes from elastic behavior, to plastic behavior and then finally to fracture (Lin et al., 2001). When polymer coating is damaged during progressive load, R_x would no longer exhibit a linear relationship with applied normal force. The failure load of a coating is interpreted based on the normal force, F_z , corresponding to the departure of R_x from linear relationship.

The scratching resistance for polymer and its composites coatings under progressive load are shown in Figures 4-5(a), (b) and (c). The x-axis and y-axis in the Figure 4-5 represents the F_z and R_x values, respectively. In Figure 4-5(a), R_x for polymer coating increases linearly with respect to F_z at the beginning of scratch. The scratching resistance curve begins to level off at about 21g of F_z , which corresponds to R_x at about 2.8g. The departure is an indication that the polymer coating has been damaged at this load.

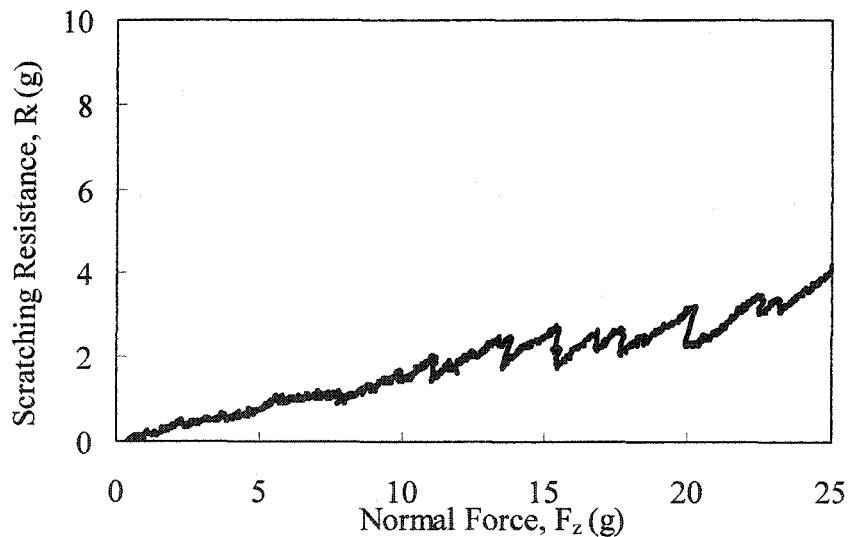
In contrast, a 10 wt% Al_2O_3 composite coating, see Figure 4-5(b), shows increasing R_x with increasing F_z up to the maximum loading of 25g. No sign of R_x departs from the linear relationship with respect to F_z . The registered value of R_x is around 4.20g under the maximum applied load, $F_{z,\text{max}}$, which is 25g. The onset of failure load for 10 wt% Al_2O_3 composite coating cannot be determined within this range of normal force.

The R_x of 10 wt% nanostructured WC composite coating displays a similar trend as the 10 wt% 50 nm Al_2O_3 composite coating but with a much steeper slope, as shown in

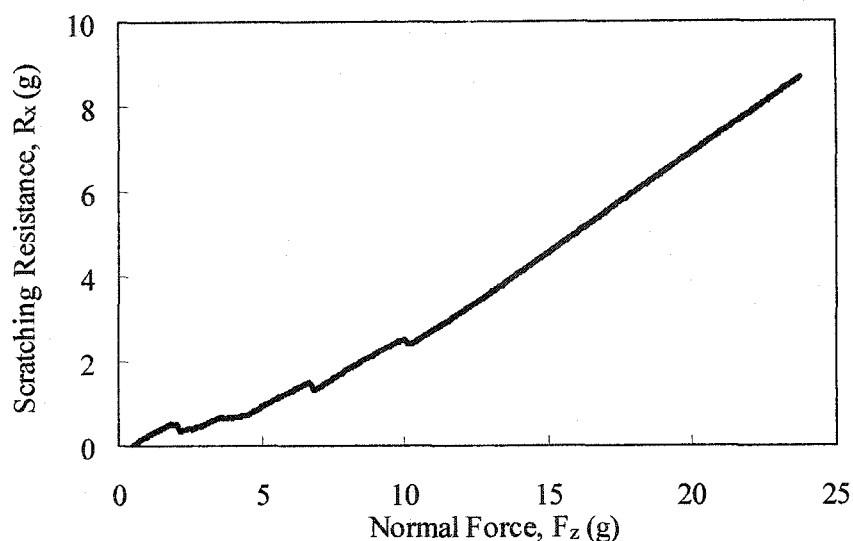
Figure 4-5(c). The R_x of 10 wt% nanostructured WC composite coating shows a linear relationship with increasing F_z up to the maximum load of 25g. The recorded R_x value at $F_{z,max}$ for 10 wt% nanostructured WC composite coating was around 9g. Again, the failure load for the 10 wt% WC composite coating and 20 wt% WC composite coating cannot be determined from this range of applied normal load.



(a) Scratching resistance of polymer coating.



(b) Scratching resistance of 10 wt% Al_2O_3 composite coating.



(c) Scratching resistance of 10 wt% WC composite coating.

Figure 4-5 Scratching resistance for different coatings under progressive load.

Table 4-1 summarizes the results of the scratching resistance of the substrate and various coatings obtained from the progressive load scratch test. Column two in this table indicates the R_x values that corresponds to $F_{z,max}$ of 25g. The asterisk shown in the table indicates the corresponding $F_{z,max}$ of polymer is 21g instead of 25g. The registered R_x at $F_{z,max}$ is used as a yardstick in order to evaluate the coating resistance to scratching. The third column lists the friction coefficient for the test samples, which was obtained from the slope of the scratching resistance curve (i.e. R_x / F_z) using linear regression method.

From Table 4-1, it can be seen that 10 and 20 wt% nanostructured WC composite coatings exhibit better scratching resistance than the polymer, 10 and 20 wt% Al_2O_3 composite coatings and substrate (steel). The scratching resistance of 20 wt% nanostructured WC composite coatings is at least three times higher than that of polymer coating. The high values of R_x as display by WC composite coatings are related to the size and content of WC particles in polymer. As the particles are sufficiently large and hard, they will form a barrier to obstruct the indenter from scratching, provided that the particles are bonded relatively strong in the polymer.

Table 4-1 Scratching resistance of the substrate and various coatings obtained under progressive load condition.

Sample	Registered R_x at $F_{z,max}$ (g)	Average friction coefficient
Substrate (steel)	7.56	0.28
Polymer	2.65*	0.13
10 wt% WC composite	8.68	0.36
20 wt% WC composite	9.74	0.42
10 wt% Al_2O_3 composite	4.20	0.14
20 wt% Al_2O_3 composite	5.95	0.19

In addition, embedded WC particles also increase the hardness of the polymer composites and minimize the penetration of the indenter during scratching. In this case, scratching resistance of WC composite coatings is more likely to be influenced by coating surface roughness. Similarly, embedded nanosize Al_2O_3 particles in polymer also improve the R_x of Al_2O_3 composite coatings. But, increase of R_x in Al_2O_3 composite coatings is not as significant as the WC composite coatings. To further investigate the effect of size on scratching resistance, a series of scratch tests were conducted for polymer composite containing Al_2O_3 particles of different sizes.

4.3.2 Friction Coefficient during Scratching

As the indenter scratches the surface under a progressive load, its frontal was continually tries to displace any barrier along the traction. At the same time, the base of the indenter was in contact with the coating. Therefore, there exist two opposing forces which are acting against the scratching direction i.e. scratching resistance and friction force. The scratching resistance is resulted from the mechanical property of the coating (i.e. hardness) whereas the friction coefficient is more of the physical property (i.e. surface roughness) of the coating.

The average friction coefficient of the substrate is 0.28, which is two times higher than polymer coating i.e. 0.13. For 10 wt% WC composite coatings, the friction

coefficient is three folds higher than polymer coatings. In addition to improving the scratching resistance of the coating, the embedded WC particles in polymer also impart the roughness of the coating. The resulted roughness is again related to the size and content of particles dispersed in the polymer. With a higher amount of particles such as 20 wt% WC composite coating, the friction coefficient increased to 0.42.

As for 10 wt% Al₂O₃ composite coating, its average friction coefficient is closed to that of the polymer coating, which is 0.14. By increasing the content of Al₂O₃ particles up to 20 wt%, surface friction coefficient reached 0.19.

4.3.3 Effect of Particle Size on Scratching Resistance

In order to investigate the effect of particle size on the scratching resistance, a comparison was made between the composite polymer coatings containing 300 nm and 50 nm Al₂O₃ particles. Again, the particles content in the coatings is 10 %. Figure 4-6 depicts the scratching resistance for composite polymer coatings containing particles of different sizes. As discussed before, the scratching resistance of 50 nm Al₂O₃ composite coating increases steadily with the applied normal load. No serious damage or fracture occurs on the surface even up to the $F_{z,max}$.

The scratching resistance curve for 300 nm Al₂O₃ composite coating is divided into two parts, i.e. 1st region and 2nd region, in order to provide better explanation regarding the sudden changes occurred during the 2nd region of the scratching. Over the 1st region, the scratching resistance curve of 300 nm Al₂O₃ composite coating displays similar characteristics as the other Al₂O₃ composite coatings, such as the stick-slip fluctuations seen in the curve. The scratching resistance for 300 nm Al₂O₃ composite coating is also slightly higher than that for the 50 nm Al₂O₃ composite coating. The slope of 300 nm Al₂O₃ composite coating increases suddenly at the 2nd region of the scratching. Unlike the 1st region, the 2nd region of the scratching resistance curve appears more like a linearly increasing straight-line with little or no fluctuation. This trend is similar to the scratching resistance curve observed in the nanostructured WC composite coatings. The occurrence of such abrupt change can be related to the surface morphology of 300 nm Al₂O₃ composite coatings. The indenter over the 2nd half of scratching could have scratched at a

relatively hard surface on the coating. Under this condition, the indenter basically slides on the coating surface.

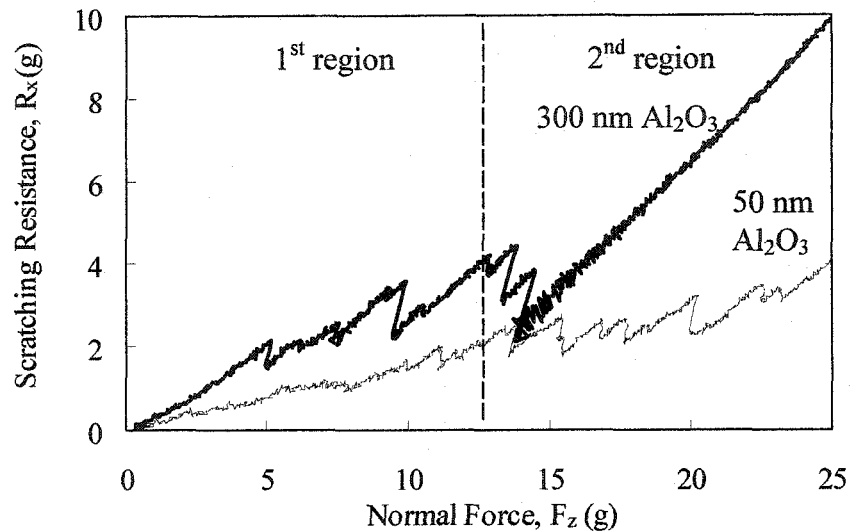


Figure 4-6 Scratching resistances of 300 nm and 50 nm Al_2O_3 particles.

4.3.4 Stick-slip Effect

Figure 4-7 shows some typical experimental plots in which the scratching resistance is shown as a function of time for three different coatings; polymer, 10 wt% 50 nm Al_2O_3 - and 10 wt% WC composite coatings. The R_x for polymer coating has less fluctuation in comparison with the other two polymers embedded with particles. Without embedded particles, the polymer coating is relatively easier to scratch than the composite coatings. This in turn dictates the mechanical property of the polymer coating which can be easily removed by scratching.

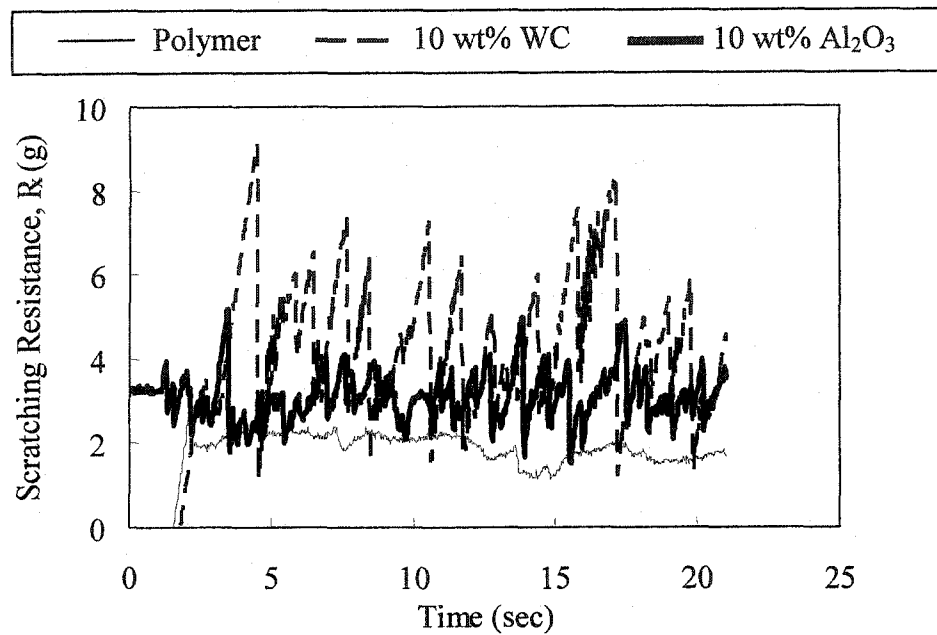


Figure 4-7 Scratching resistance versus time at applied constant load.

More obvious traditional stick-slip patterns are observed in the 10 wt% Al₂O₃ composite coating. The embedded Al₂O₃ particles in the polymer matrix act as a barrier towards scratching. During the scratching, the indenter was driven through an elastic mechanism, which is the stick stage. Indenter and coating will stick together until the elastic forces became sufficient to jerk them loose and then sliding happens (Zhang et al., 2002) The R_x builds up to a maximum during the stick stage and drops during the slip stage. The cycle will keep repeat itself and eventually result in the fluctuations (i.e. stick-slip pattern) seen in the plots.

In the case of 10 wt% WC composite coatings, the stick-slip pattern becomes more prominent than in the 10 wt% Al₂O₃ composite coating. In this case, the indenter has to drive through a greater barrier when the particles become coarser and harder. When particles are getting sufficiently larger and harder, they will obstruct the indenter from scratching.

4.3.5 Relationship between Scratching Resistance and Hardness

Figure 4-8 below shows the relationship between the scratching resistance and microhardness of polymer and its composite coatings. From this figure, it can be seen that the scratching resistance of polymer coatings is strongly dependent on their hardness, which in turn depends on the amount of particles embedded in the coatings.

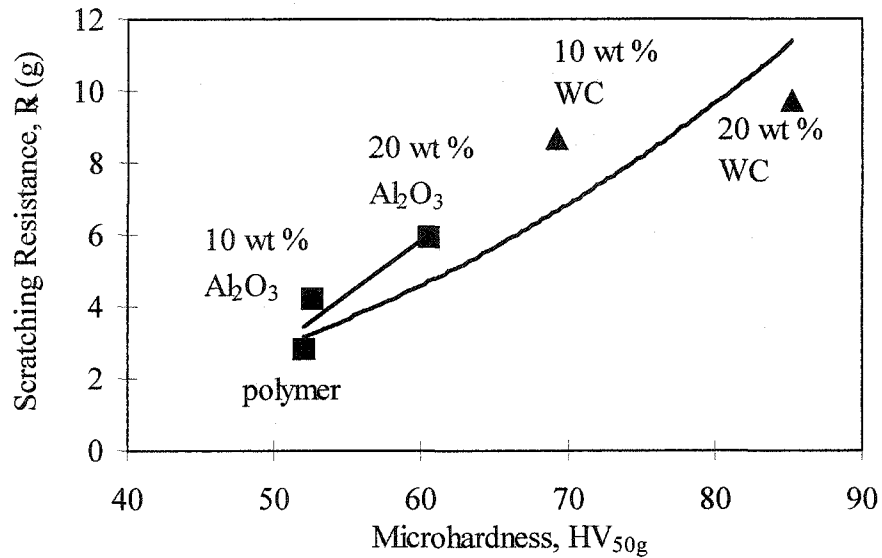


Figure 4-8 Relationship between scratching resistance and microhardness.

4.3.6 Mechanism of Deformation

In a deformation process such as scratching, there are several mechanical factors which may influence the fracture and removal of polymer or its composite coatings. One of these experimental variables is the angle of the indenters. The imposed contact geometry may play a role in regulating the strain of the contact. Moreover, other vital factors in defining the severity and features of deformation include the applied normal load, velocity of scratching, local temperature of the contact surface (Briscoe, 1998) and the type of polymer (Xiang et al., 2000).

Figure 4-9 depicts the deformation mechanism on coating surface during scratching. At time 0 the indenter is in contact with the coating surface (point a). No scratch happens at this point. As the indenter moves along the surface, the indenter slowly penetrates into

the coating with increasing the applied normal force (point b). Both elastic and plastic deformation can occur in this region. As the normal load reaches above the critical load (point c), the line starts to level off with the signs of fluctuation indicating that severe fractures occurred on the scratched surface. At point c, the damaged coatings may experience adhesion failure and eventually be displaced from the traction. When the applied normal force exceeds the threshold of the coating, the indenter will penetrate into the coating and eventually scratch the substrate. As a result, another sharp increase in the scratching resistance curve will occur at point d which is the scratching resistance of the substrate (metal).

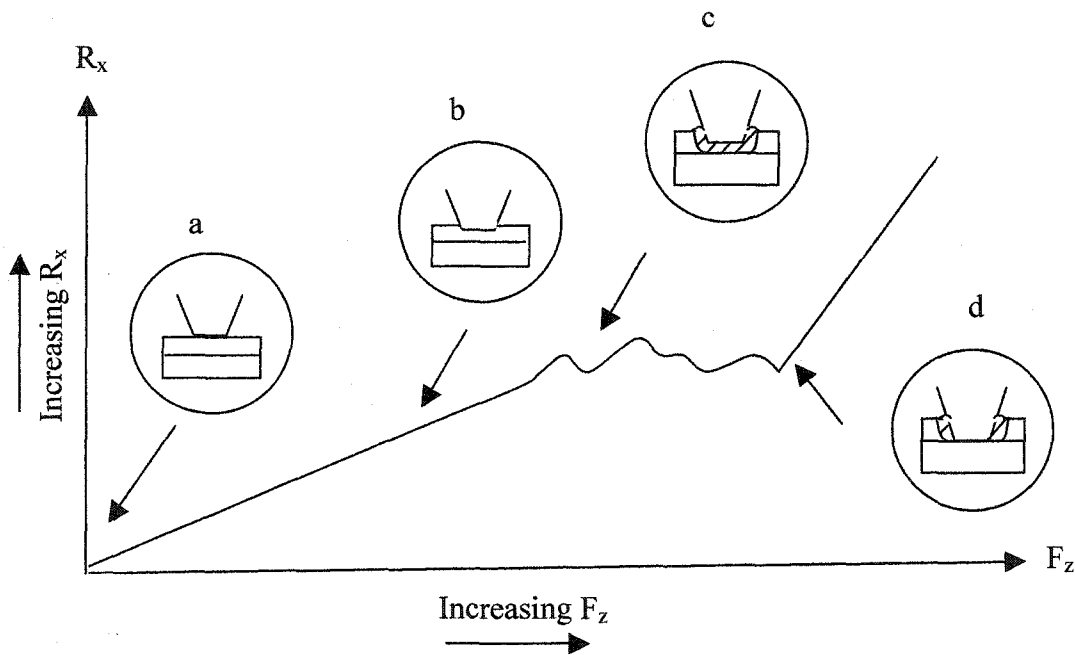


Figure 4-9 Front view of the indenter during scratching.

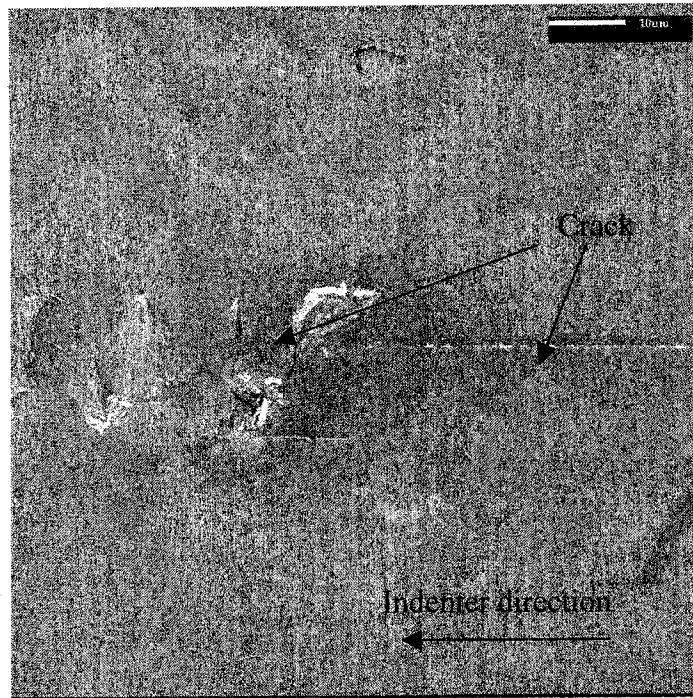
4.3.7 Scratched Surface of Coatings

In general, the shape of the scratch tracks can serve as an indicator for the severity of wear during deformation as well as the mechanism behind the scratching damage. Therefore, a more detailed observation of the scratch pattern was studied under SEM. The scratched track created on the polymer coating during progressive scratch test is shown in Figure 4-10(a). From Figure 4-10(a), the scratch track is initially seen as well-defined edges on the sides of the scratch groove. However, this scratch pattern changes

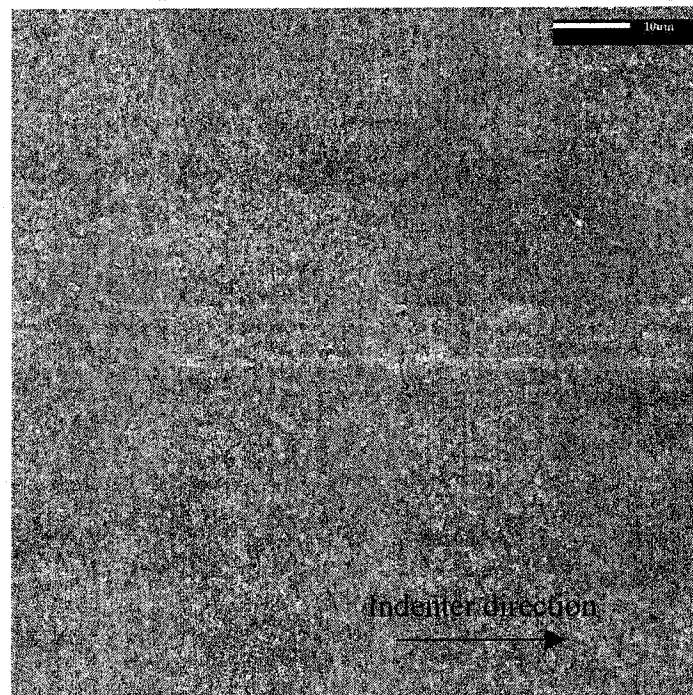
abruptly when the load reaches the threshold of the polymer coating. The polymer coating is forced by sliding the indenter into a more localized stress fields hence causing initiation of cracks in front of the indenter. The impact of the indenter on the polymer coating has resulted in a significant plastic deformation with formation of deep groove and cracks. The cracks penetrated into the coating due to the tearing action of the indenter on the surface. Following the impact, the indenter may “jump” from its original position and land onto another position. As the indenter keep scratching, the sequential accumulation of tangential force causes the squeezing of the polymer accumulates in front of the indenter until it reaches the plastic limit and finally lead to the zigzag pattern normal to the direction of the indenter movement.

As for 10 wt% Al₂O₃ composite coating, the scratch track is less visible than the polymer coating, see Figure 4-10(b). The deformation of 10 wt% Al₂O₃ composite coatings is related to the ploughing mechanism, resulted by ductile flow of the polymer around the indenter tip. The ductile ploughing may occur without any evidence of discrete failure and may be accompanied by a significant viscoelastic recovery at the rear of the contact region. As a result, well-defined edges form on both sides of the scratch grooves.

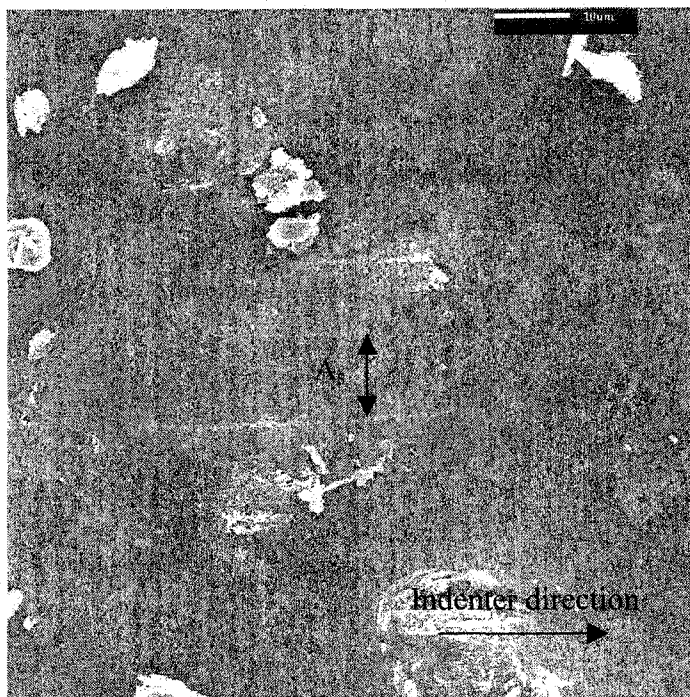
Figure 4-10(c) shows the scratch track of the nanostructured 10 wt% WC composite coating. The scratch track appearance of 10 wt% WC composite coating is hardly visible from the SEM micrograph. The width of scratch track, A_s is measured to ensure the scratch track is consistent with the indenter width. From the picture, A_s is 10 μm wide and match the width of the indenter. Comparing the scratch track in Figure 4-10(c) to Figure 4-10(a) and (b), the former shows no obvious damaged on the coating surface. The applied maximum load from the scratch test does not cause significant damage on the 10 wt% nanostructured WC composite coating compare to the case of the polymer coating. In this case, no detectable permanent deformation is seen except for ‘ironing’ effect of the original surface asperities on the coating surface.



(a) Surface morphology of scratch track on polymer coating.



(b) Surface morphology of scratch track on 10 wt% Al₂O₃ composite coating



(c) Surface morphology of scratch track on 10 wt% WC composite coating.

Figure 4-10 SEM micrographs show the images of the scratch tracks on coatings under progressive load condition.

The results presented in this section lead us to conclude that, scratching resistance increases with increasing normal force, F_z . When the F_z reaches the threshold of a coating, the normal force will cause damage to the coating. It can be seen that the R_x of polymer coating is not as scratch resistance as polymer with embedded particles. The continual loading damaged polymer coating before F_z reached its maximum load. On the other hand, all the composite coatings, including 50 nm and 300 nm Al_2O_3 -, and WC composite coatings, show increasing R_x with increasing F_z up to maximum load. No significant fracture or cracking occurred on these composite coatings. Embedding particles in polymer can strengthen and enhance mechanical properties such as microhardness and scratching resistance of the polymer coatings.

4.4 TABER ABRASION TEST

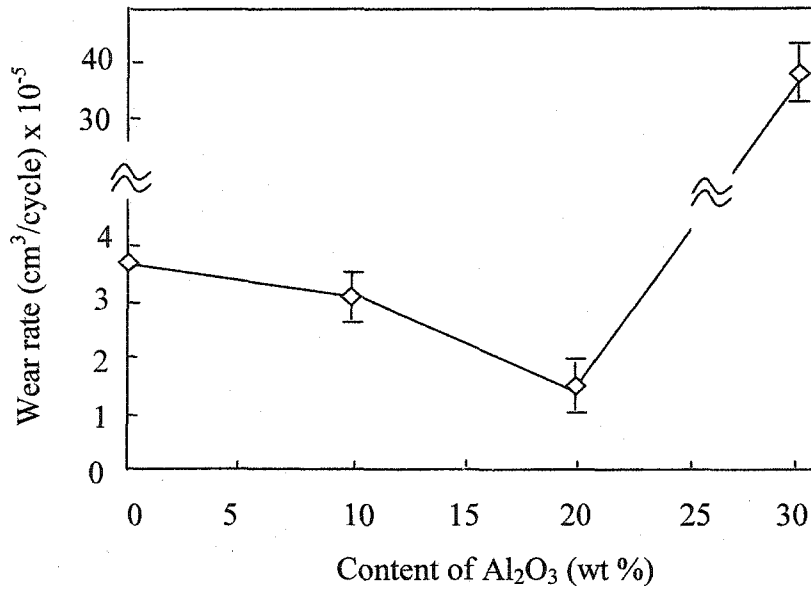
Taber abrasion test is the most commonly accepted standard lab test to evaluate the resistance of coatings to abrasion. In the Taber abrasion test, a coated panel turns under two rotating abrasive wheels. With this configuration, a characteristic rub-wear action was produced when the sample was turning on a vertical axis against the sliding motion of the two abrading wheels which move in the opposite directions. The resulting abrasion formed a pattern of a complete circle on the test sample, over an area approximately 30 cm².

4.4.1 Abrasive Wear

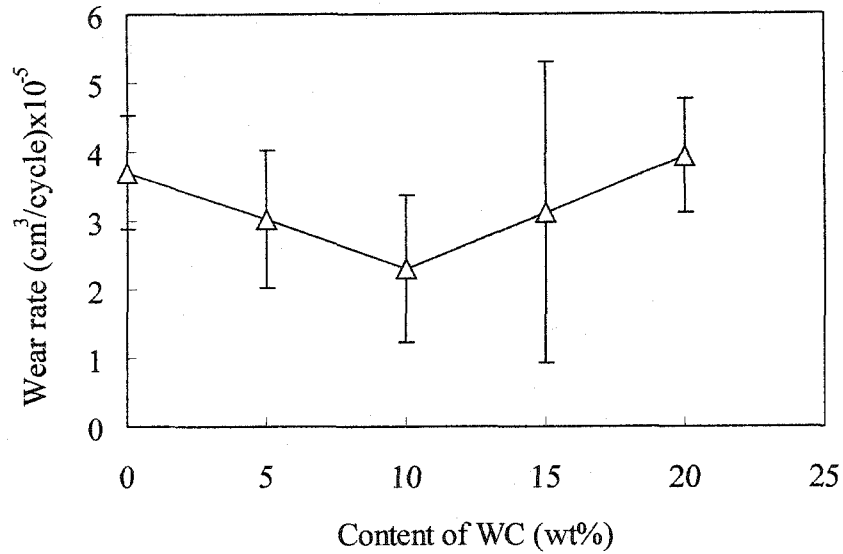
Figure 4-11 displays the wear rate in unit volume loss (cm³) of the samples per rotating cycle versus the content of particles in the polymer. Figure 4-11(a) shows the wear rate of Al₂O₃ composite coatings. From the graph, it is evident that the wear rate of 10 wt% Al₂O₃ composite coating is lower than the polymer coating. A minimum wear rate occurs at a content of 20 wt% Al₂O₃ particles. However, further increasing the amount of Al₂O₃ particles in the polymer could result in an increased abrasive wear. At a Al₂O₃ particle content of 30 wt%, for example, the composite coating displays a significant increase in wear rate. The wear rate in this case is higher than that for the polymer coatings. The sudden increase in wear rate of 30 wt% Al₂O₃ composite coating may be attributed to the excessively high amount of particles in the polymer. When the amount of particles is too high, there is insufficient polymer to bond the particles together in the polymer matrix. As a result, a weak adhesion between the polymer with particles and polymer with substrate is anticipated.

Similarly, a minimum wear rate is observed in Figure 4-11(b) for WC composite coatings. The minimum wear rate occurs at 10 wt% WC content. The wear rate for WC composite coatings starts to climb up beyond the content of 10 % WC particles. At content of 20 % WC particle, the wear rate becomes similar to that of polymer coating. The result obtained for 20 wt% WC composite coating in Taber abrasion test is not consistent to the result obtained from scratch test. Based on scratch test, scratching resistance of WC composite coating increases with increasing content of particle. But, in

Taber abrasion test wear resistance of WC composite coating decreases beyond particle content of 10 wt%. A possible reason is that the wear mechanism of scratch and Taber abrasion test are different from each other, which causes dissimilarity in predicting the mechanical property of WC composite coatings.



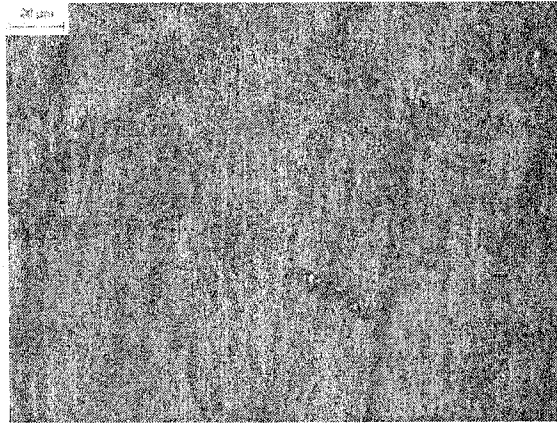
(a)



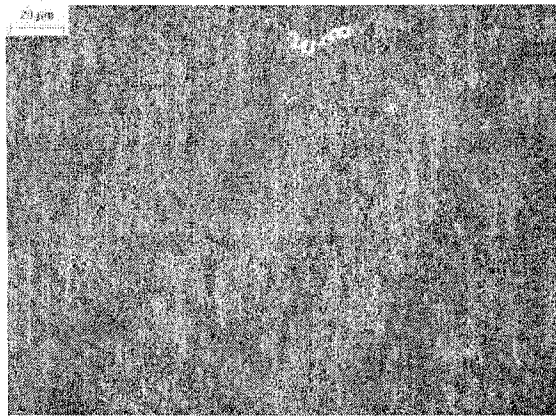
(b)

Figure 4-11 Wear rates of (a) Al₂O₃ composite coatings and (b) nanostructured WC composite coatings obtained from Taber abrasion test.

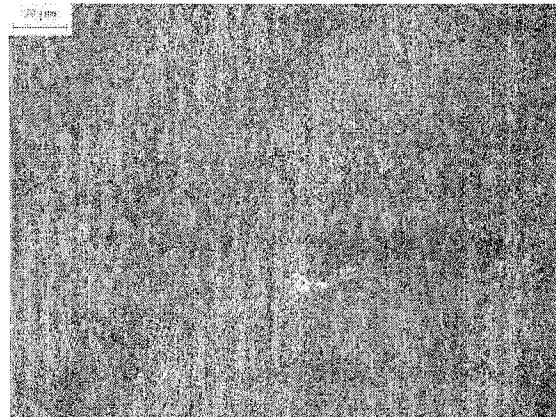
A series of wear tracks for the polymer and Al₂O₃- containing polymer composite coatings are shown in Figure 4-12. The pictures are arranged from the highest wear loss to the lowest wear loss. It is evident that the depth of the wear tracks decreases from high to low wear loss. The visibility or depth of the wear tracks is an indication to the wear level. A deeper wear track means that the coating is less resistance to the abrasion wear and vice versa.



(a)



(b)



(c)

Figure 4-12 A unique “X” pattern of abrasion is produced by the rotary rub-wear action of the wheels. The abrasion marks are deeper in (a) polymer, and become less visible in 10 wt% Al_2O_3 (b) and 20 wt% Al_2O_3 (c) polymer composite coatings.

4.4.2 Mechanism of Abrasive Wear

The difference between scratch test and Taber abrasion test lies on the mode of contact between asperities. Since the scratch test is really a contact between a single asperity with coating surface, it truly differs from Taber abrasion test that involves multiple asperities contact. During Taber abrasion test, protruding WC particles on the coating surface were dislocated from its surface layer. These loosen WC particles will stay on the traction that is being abraded by the turning abrasive wheels. Since they are unable to escape from the traction, these particles eventually act as abrasive that accelerate the wear of the coating, see Figure 4-13.

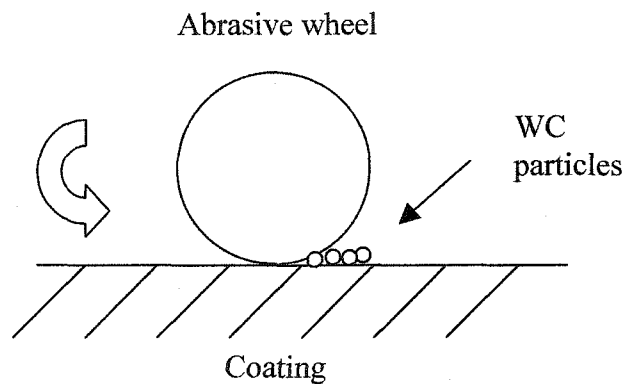


Figure 4-13 Combined action of loosen particles and abrasive wheel on composite coating surface during Taber abrasion test.

4.5 ELECTROCHEMICAL TEST

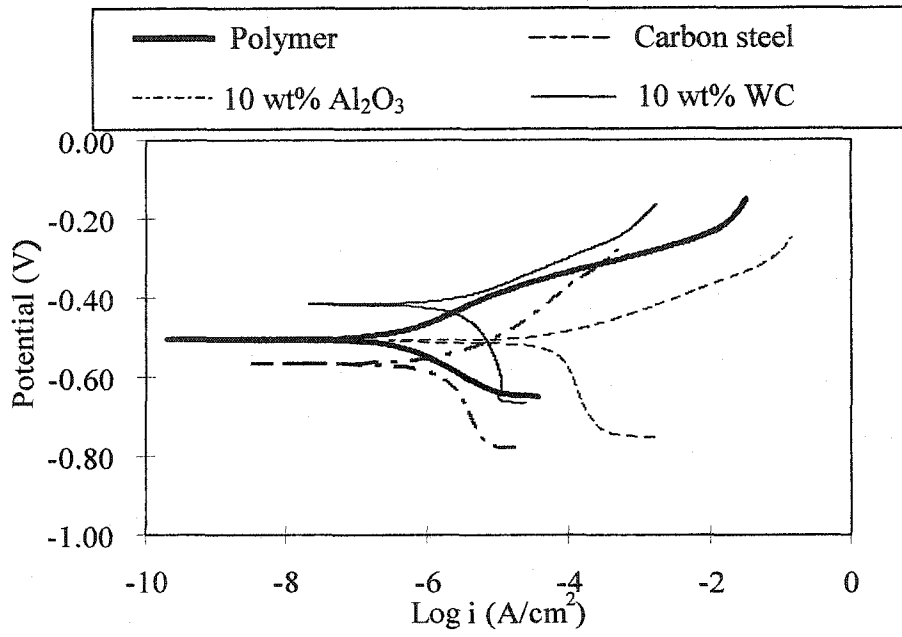
Potentiodynamic Polarization of Coatings

The electrochemical properties of carbon steel and coatings are studied by potentiodynamic polarization technique. The applied sweeping potential ranges from -0.25 V to +0.25 V versus E_{corr} in order not to damage the coatings.

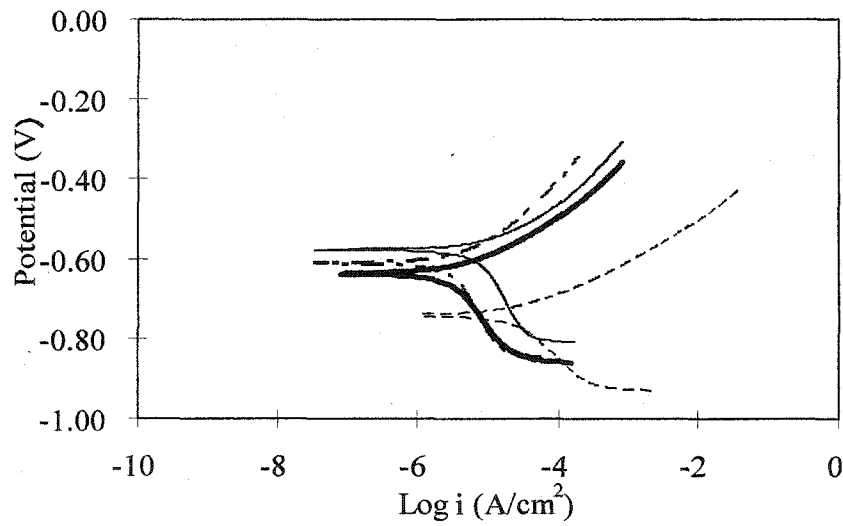
Figure 4-14 depicts a series of potentiodynamic polarization curves of carbon steel, polymer and 10 wt% - Al₂O₃ and WC composite coatings at different time intervals. At the beginning of polarization scan (Figure 4-14(a)), the current density, i_{corr} of carbon steel is about 100 times larger than the polymer coating, follows by 10 wt% Al₂O₃ composite coating and finally 10 wt% WC composite coating. The low i_{corr} values for polymer and its composite coatings indicate that these coatings are less susceptible to corrosion than bare carbon steel. This noble property of polymer and its composite coatings have served to minimize the corrosion rate of coated carbon steels.

After two hours of immersion, the current density of carbon steel in the potential range of -0.20 V and -0.90 V is slightly lower than those at the beginning of test (Figure 4-14(b)). At that time, the surface of carbon steel was already covered with oxide layer. It is very likely that the formation of oxide layers has formed a diffusion barrier on carbon steel surface and indirectly reduced the dissolution of metal. When mass transportation of metal ions is slowed down, as a consequence, corrosion rate is subdued. Since corrosion rate is directly proportional to i_{corr} , decrease in corrosion current density indicates decreasing corrosion rate. Also shown in the Figure 4-14(b), the current densities of 10 wt% - Al₂O₃ and WC composite coatings have becomes similar to that for polymer coating.

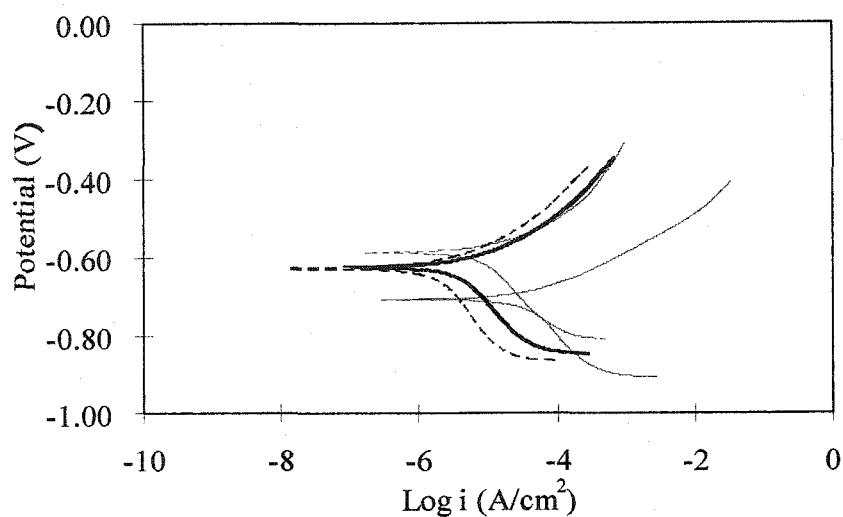
To further intensify the damage that might be caused by corrosion, the samples were immersed in the solution for another 22 hours. The polarization curves at 24th hour are shown in Figure 4-14(c). From the graph, it can be seen that the current density of carbon steel, polymer and 10 wt% - Al₂O₃ and WC composite coatings remained much the same as those from the last 22 hours. The samples, especially coatings exhibited a stable electrochemical response.



(a)



(b)



(c)

Figure 4-14 Potentiodynamic curves for different coatings at (a) beginning (b) 2 hours later and (c) 24 hours later in 3 wt% NaCl solution.

The anodic and cathodic regions of polarization curve were extrapolated to retrieve E_{corr} and i_{corr} of samples and the data are shown in Figure 4-15 and Figure 4-16 respectively. Figure 4-15 depicts the E_{corr} of carbon steel, polymer and 10 wt% - Al_2O_3 and WC composite coatings as a function of time. From thermodynamic point of view, the E_{corr} is an indication for the driving force of corrosion potential.

At time 0, the E_{corr} of carbon steel is at -0.51 V and dropped to -0.75 V after half hour. Afterwards, the E_{corr} of carbon steel is relatively stable throughout the course of potentiodynamic measurement. As for the E_{corr} of coatings, polymer has E_{corr} closed to the carbon steel in the beginning of experiment. After half an hour the E_{corr} of polymer dropped to -0.64 V. From here, the polymer has reached equilibrium with the aqueous system. The E_{corr} of polymer is very stable throughout the test. The 10 wt% - Al_2O_3 and WC composite coatings also exhibit similar behavior as the polymer. Other composite coatings which are not shown in the graph (i.e. 5 wt% - Al_2O_3 and WC, 20 wt% - Al_2O_3 and WC composite coatings) showed similar corrosion behaviors as polymer with their E_{corr} within the range of $\pm 0.10\text{V}$ of the E_{corr} for polymer.

Figure 4-16 depicts the corrosion current density, i_{corr} as a function of time for the carbon steel and coatings. From Figure 4-16, i_{corr} of the carbon steel at any time of the test is the highest, $10^{-4} \text{ A/cm}^2 \sim 10^{-4.5} \text{ A/cm}^2$, compare to the polymer and Al_2O_3 composite coatings. The carbon steel showed a drop in i_{corr} over the first half hour in the electrolyte solution, possibly due to the formation of oxide layers on carbon steel surface. The oxide layers create a barrier between metal and corrosive solution. Unlike carbon steel, the i_{corr} for both coatings increased from 10^{-6} A/cm^2 to $10^{-5.5} \text{ A/cm}^2$ after half hour in solution. Their current then becomes relatively stable. For 10 wt% WC composite coatings, similar i_{corr} versus time behavior as the polymer and Al_2O_3 composite coatings was observed except that its i_{corr} is slightly higher than that for the polymer and Al_2O_3 composite coatings. This marginal difference is probably caused by the morphology of WC particles in the polymer after heat treatment, referred to Figure 4-1(d). The clustered WC particles were visible on the coating surface. The protruded or exposed WC particles may create a circuitry path for the electrolyte to migrate from the surface to the substrate. Therefore, the i_{corr} of the WC composite coatings is slightly higher than those of the polymer as well as Al_2O_3 composite coatings. Other Al_2O_3 composite coatings (i.e. 5 and 20wt %) has i_{corr} values closed to the i_{corr} of polymer, in contrast to i_{corr} around 10^{-5} A/cm^2 for the WC composite coatings (i.e. 5 and 20 wt%).

Based on the above discussion, it was concluded that embedment of nanoparticles in polymer matrix will not sacrifice the corrosion resistance of the polymer itself.

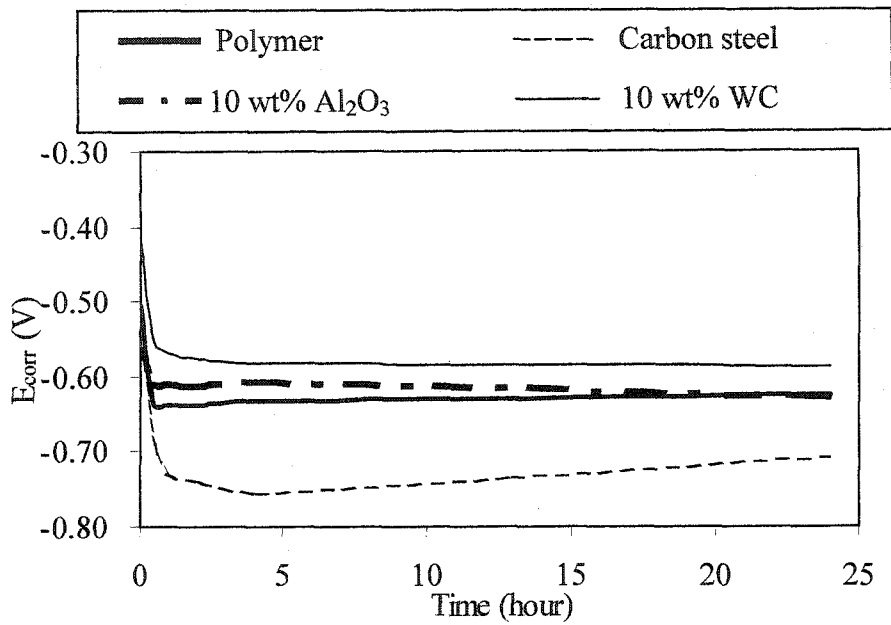


Figure 4-15 Variation of corrosion potential of coatings with immersion time in 3 wt% NaCl.

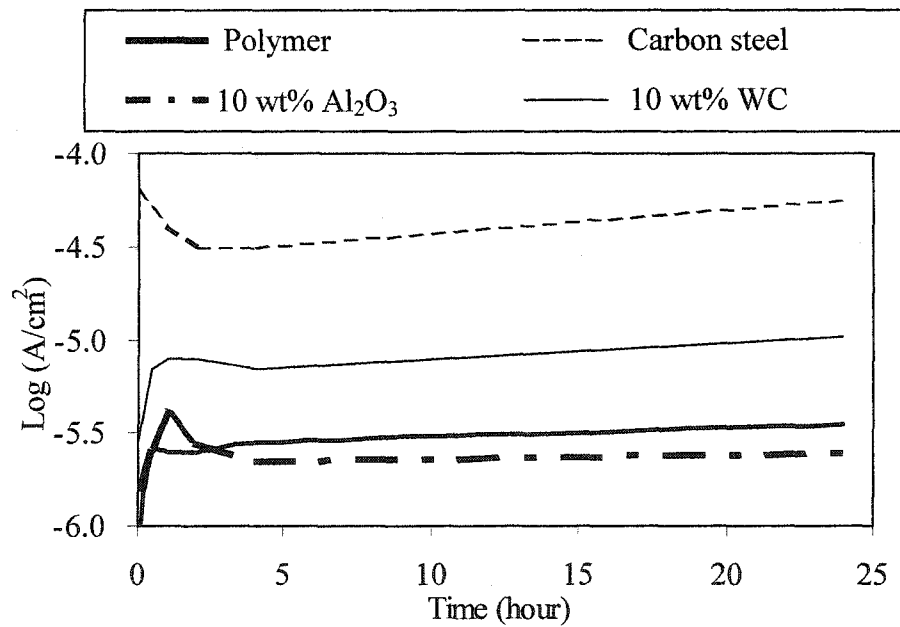


Figure 4-16 Corrosion current density of composite coatings varies with time in 3 wt% NaCl.

4.6 EROSION-CORROSION TEST

4.6.1 Volume Loss for Carbon Steel, Polymer and Polymer Composite Coatings

The performance of the carbon steel, polymer and its composite coatings in a slurry pipeline condition is further investigated by conducting a simulated erosion-corrosion (E-C) test in the specially designed cell shown in Figure 3-8. The volume loss obtained in this test is the average of three to four samples.

Figure 4-17 presents the volume loss during the E-C test. For a duration of 6-hour E-C tests, carbon steel experienced the highest volume loss as seen in Figure 4-17 (a). Without a protective film, surface of carbon steel is being eroded continuously in the solution. The exposed surface of carbon steel was continually removed due to microploughing and microcutting actions from impingement of sand particles. In addition to erosion, corrosive environment also contributes to the observed volume loss. As discussed earlier, corrosion develops a film or thick layer of corrosion products on carbon steel surface, minimizing further corrosion. However, under the erosion condition the so-called 'protective film' is removed by erosion, which allows corrosion to proceed rapidly. The interactive cycle between erosion and corrosion speeds up the failure of carbon steel (e.g. become thinner) and undercuts the surface with grooves and pits, as shown in Figure 4-18.

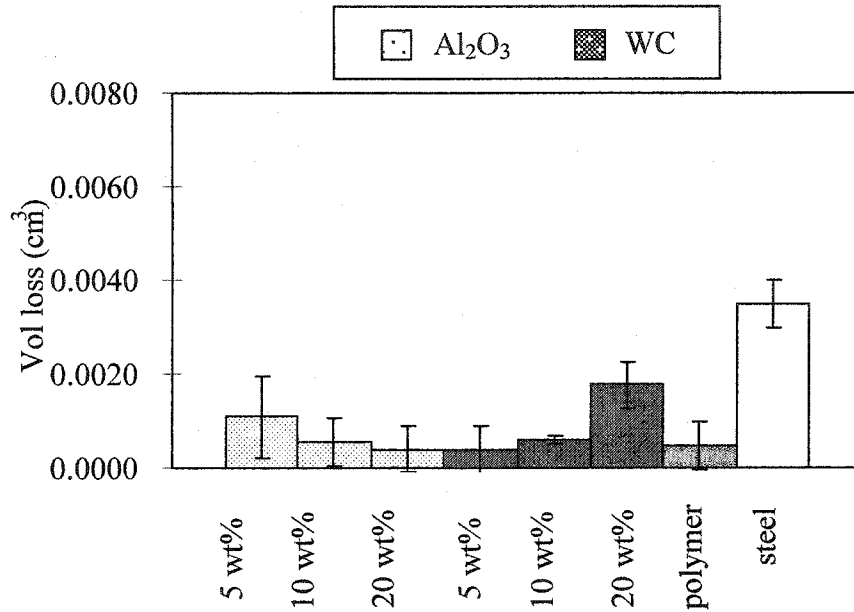
To minimize the damage of carbon steel under erosive and corrosive environment, polymer or reinforced polymer is coated on the carbon steel surface. As shown in Figure 4-17, volume loss of carbon steels coated with either polymer or its composites was reduced tremendously as compared to volume loss of bare carbon steel. Even though polymer and its composite coatings have lower hardness than carbon steel, their high elasticity has certainly played an important role to improve E-C resistance. The elastic property of polymer and its composite coatings appears to adsorb the impact from the bombarding sand particles, hence minimizing the removal of the coating layers into the slurry.

Among the coated surfaces, the volume loss of 20 wt% WC composite coating is the highest followed by the 5 wt% Al₂O₃ composite coating. The rest of the coatings exhibit more or less the similar volume loss of about 0.0005 cm³. The bar chart also depicts a certain trend within the Al₂O₃ and WC composite coatings in the context of their particle content in the polymer. The volume loss for Al₂O₃ and WC composite coatings is ranked from lowest to highest in the following order, respectively: 20 wt% < 10 wt% < 5 wt% and 5 wt% < 10 wt% < 20 wt%. The explanation for this phenomenon will be discussed later in this chapter.

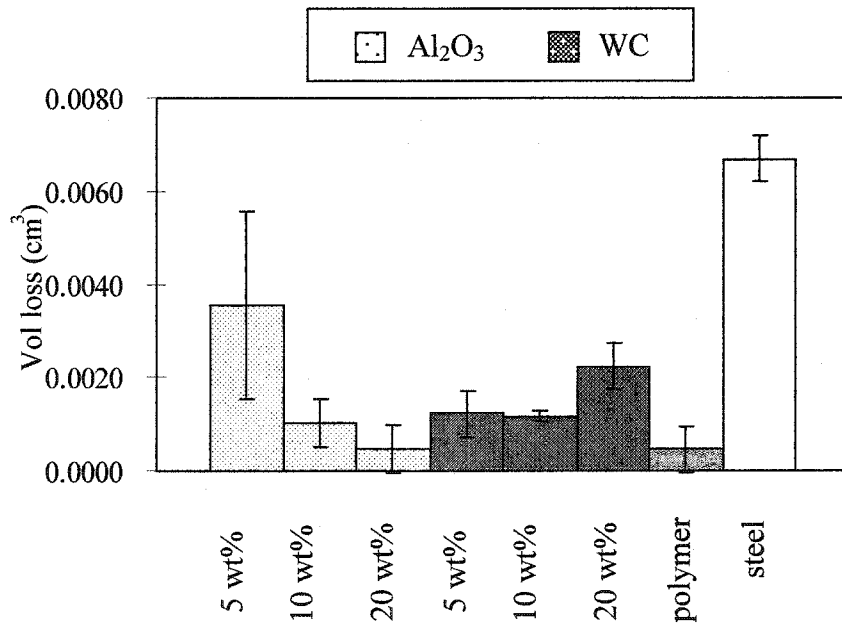
To show a more significant difference between the polymer and its composite coatings, E-C tests were extended for another 6 hours. The results from the extended E-C tests are shown in Figure 4-17 (b). As anticipated, bare carbon steel suffers the highest losses in volume among the samples tested. Also shown in this figure is that polymer experienced the lowest volume loss. The relatively high elasticity of polymer in comparison with its composites coatings eventually works better in erosive and corrosive environment.

After experiencing an extended E-C test, 5 wt% Al₂O₃ composite coating showed the highest volume loss among all the coated samples. The visual inspection revealed that one of the 5 wt% Al₂O₃ composite coating samples was wear off during the test, leaving the substrate exposed to the erosive and corrosive environment.

As for other Al₂O₃ composite coatings, the volume loss of 10 wt% Al₂O₃ composite coating is about one third of 5 wt% Al₂O₃ composite coating, whereas 20 wt% Al₂O₃ composite coating is around a quarter of the 5 wt% Al₂O₃ composite coating. These results appear to suggest that increasing Al₂O₃ content in the polymer decreases volume loss of Al₂O₃ composite coatings. Again, the E-C resistance of Al₂O₃ composite coatings corresponds to the ranking obtained in 6-hour E-C test. Figure 4-19 shows traces of grooves or waves on a 10 wt% Al₂O₃ composite coating surface after 12 hours E-C test. The surface of the coating was wore away by a stream of sand particles which strikes and rebounds from the surface.



(a) Volume loss for polymer and its composite coatings after 6 hours exposure in E-C test.



(b) Volume loss for polymer and its composite coatings after 12 hours exposure in E-C test.

Figure 4-17 Volume loss of polymer and its composites coatings in a simulated erosive and corrosive environment.

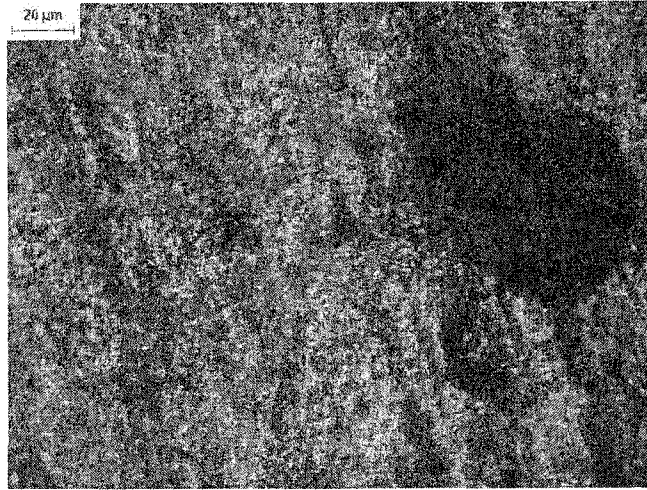


Figure 4-18 Carbon steel surface covered with pits and grooves after E-C test.

With regards to the WC coatings, the 5 and 10 wt% WC composite coatings exhibit almost the same volume loss. As the content of WC particles is increased to 20 wt%, higher volume loss is obtained from the test. In fact, the average volume loss of WC composite coatings is relatively higher than Al_2O_3 composite coatings. The volume loss of WC composite coatings is largely affected by particles distribution on coating surface. As previously shown in Figure 4-1(d), WC particles were indeed exposed to the environment. These protruded WC particles reduced their effective areas for bonding with polymer. In fact, it is extremely difficult to achieve good adhesion between PTFE and reinforcing entities since PTFE is the most chemically inert fluorocarbon. As the consequences of insufficient bonding with polymer, many of protruded WC particles are eroded during E-C test. Figure 4-20 shows the ‘smothering’ effect on the surface of 10 wt% WC composite coating after removal of exposed WC particles. A detail illustration of erosion mechanism for WC composite coatings is shown in Figure 4-21. Therefore, with higher amount of WC particles, E-C resistance tends to depreciate because more particles are exposed on coating surface.

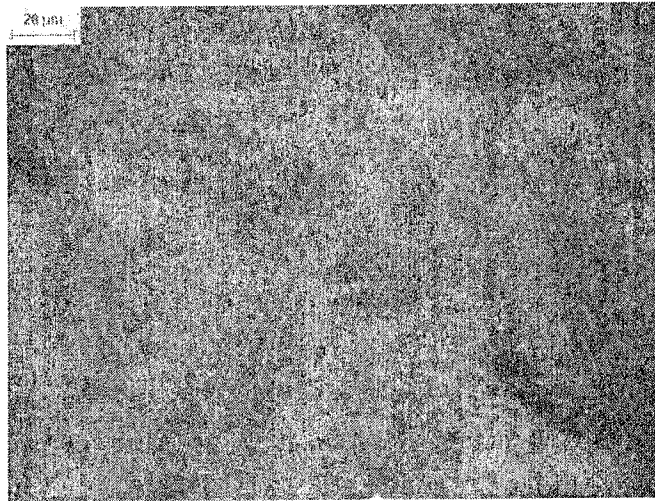


Figure 4-19 Wavy surface of 10 wt% Al₂O₃ composite coating after twelve hours exposure in E-C test.

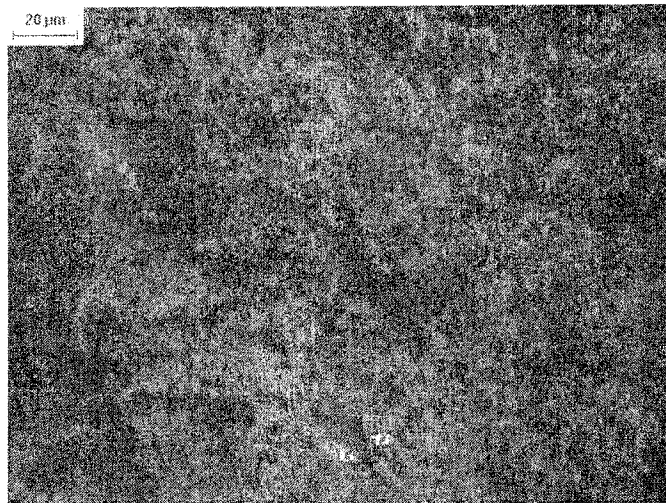


Figure 4-20 Surface of 10 wt% WC composite coating after 12 hours exposure in E-C test. The surface is 'smoother' than that before E-C test.

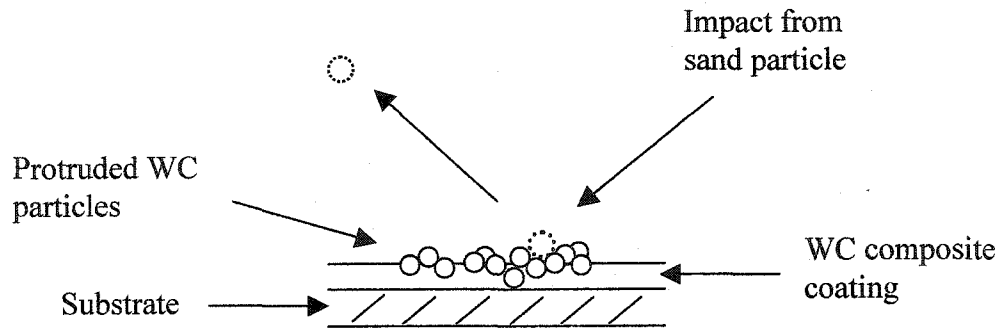


Figure 4-21 Weak bonding between protruded particles and polymer is detrimental to the composite coating. The protruded particles are likely to be removed from the coating surface due to the impact from impinging sand particles.

4.6.2 Comparison between GemThane and Xylan 1810

In order to examine the role of polymer binding with particles and substrate in surface protection, a different polymer, GemThane is used in the E-C test. GemThane and the reinforced GemThane with 10 wt% Al_2O_3 nanoparticles are studied under the same E-C test condition used for as Xylan 1810.

The results are summarized in Table 4-2 and Table 4-3, for GemThane and Al_2O_3 reinforced GemThane, respectively. Table 4-2 shows that one out of four GemThane samples, which is denoted as GemThane C, suffered a severe weight loss (0.029 g) because the coating was detached from the substrate after 12 hours E-C test. For the rest of the samples, an average weight gain of 12 mg after 12 hours E-C test was observed. Visual inspection showed some blister on the coating surfaces. By further extending the E-C test for additional 4 hours, all the GemThane coatings were detached from the substrates.

Table 4-2. Weight of GemThane polymer before and after E-C test.

Legend	Initial weight (g)	After 12 hours (g)	After 16 hours
GemThane A	10.6425	10.6432	Adhesion failure
GemThane B	10.6532	10.6550	
GemThane C	10.6638	10.6346	
GemThane D	10.0932	10.0946	

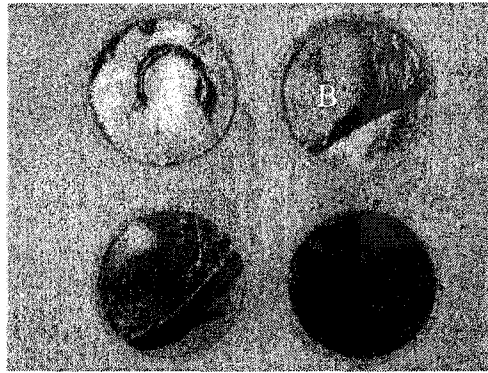
Table 4-3. Weight of 10 wt% Al₂O₃ in GemThane before and after E-C test.

Legend	Initial weight (g)	After 12 hours (g)	After 24 hours
Al ₂ O ₃ - GemThane A	10.6629	10.6630	Adhesion failure
Al ₂ O ₃ - GemThane B	9.8606	9.8612	
Al ₂ O ₃ - GemThane C	10.0984	10.1053	
Al ₂ O ₃ - GemThane D	9.5110	9.5125	

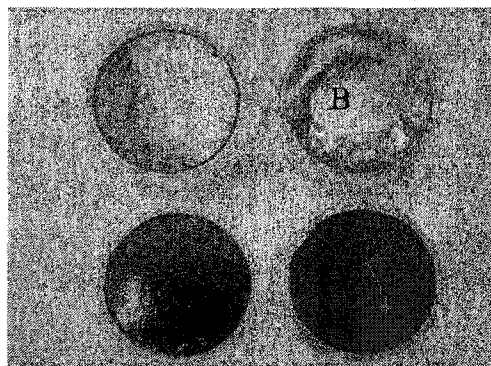
For the 10 wt% Al₂O₃ reinforced GemThane samples, results in Table 4-3 showed a negligible weight loss. Almost all the samples registered a slight increase in weight after a 12 hours E-C test. The total E-C time for Al₂O₃ reinforced GemThane coatings to detach from the substrates increased to 24 hours. The reinforced polymer may have slightly prolonged the protection on substrate for few more hours. The failure of adhesive joints of GemThane and Al₂O₃ reinforced GemThane coatings after 16 and 24 hours of E-C test, respectively, as shown in Figures 4-22(a) and (b) suggests that use of Al₂O₃ reinforced GemThane coating for E-C protection is not realistic.

Whenever an adhesive failure occurred, degradation of the interface between the substrate and the polymer was found to be a major cause of failure. This study also reveals that the joint failure is due to aging and water absorption into the polymer as illustrated by the apparent weight gain recorded for GemThane and Al₂O₃ reinforced GemThane coatings. In general, polyurethane possesses a strong polarity and favors formation of hydrogen bonding (Szycher, 1999). Therefore, it has the tendency to absorb water often up to an equilibrium concentration from surrounding environment. The

processes involved ranges from adsorption, diffusion, to dissolution. The absorbed liquid tends to reduce the adhesion between the coating and substrate. This observation was not surprising, given that other experiments have shown that coating adhesion is particularly susceptible to attack by water (Crossen et al., 1998; Knox and Cowling, 2000).



(a) GemThane polymer after 16 hours exposure in E-C test. A: GemThane A, B: GemThane B, C: GemThane C, D: GemThane D.



(b) 10 wt% Al₂O₃-GemThane polymer after 24 hours exposure in E-C test. A: Al₂O₃-GemThane A, B: Al₂O₃-GemThane B, C: Al₂O₃-GemThane C, D: Al₂O₃-GemThane D.

Figure 4-22 Pictures showing the adhesion failure joints between the coatings and substrates.

In comparison, Xylan 1810 shows far superior properties than GemThane in most of the applications. The Xylan 1810 coating remain intact to the substrates after 53 hours of E-C test as shown in Figure 4-23.

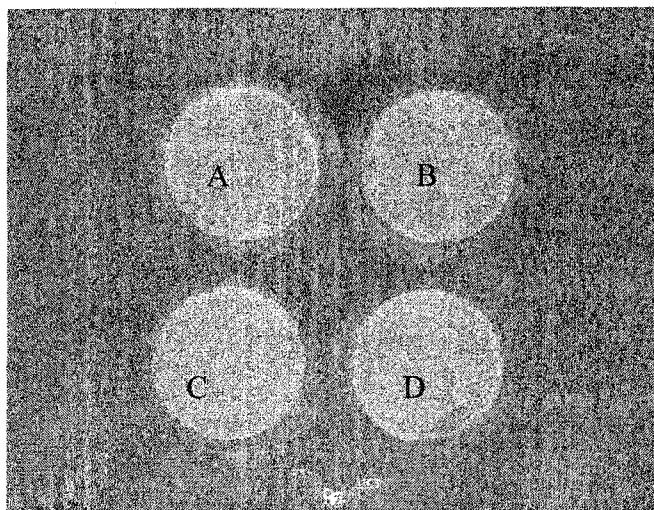


Figure 4-23 Xylan 1810 coatings after 53 hours exposure in of E-C test. All the samples A, B, C and D were subjected to the same condition of preparation and E-C test.

Based on the results, Xylan 1810 coatings have better E-C resistance than GemThane or Al_2O_3 reinforced GemThane coatings. GemThane coatings, without the addition of any particles show higher weight gain or detach faster from the substrates. On the other hand, Al_2O_3 reinforced GemThane coatings are slightly better than GemThane coatings with less weight gain after the 12 hours E-C test and detach after 24 hours. Those embedded Al_2O_3 nanoparticles in the coatings may fill up some volume of the polymer and resulted in less water absorption per surface area hence extended the E-C lifetime of the coatings up to a certain degree.

CHAPTER 5 CONCLUSIONS & RECOMMENDATIONS

FOR FUTURE WORK

5.1 CONCLUSIONS

- 1) The embedded particles in polymer matrix have enhanced certain properties of the polymer such as microhardness, scratching resistance and abrasion resistance. The enhanced properties of composite coatings are largely affected by the particle size, content of particles and particle distribution in polymer matrix.
- 2) WC composite coatings exhibit higher microhardness and scratching resistance than corresponding polymer coatings. Scratching resistance of the nanostructured WC composite coatings is at least three times higher than the polymer coatings. Similarly, the 50 nm Al_2O_3 composite coatings show a slight increase in microhardness and scratching resistance. But the 300 nm Al_2O_3 composite coatings have microhardness and scratching resistance similar to that as the 10 wt% WC composite coatings.
- 3) Taber abrasion test shows that 20 wt% Al_2O_3 composite coating and 10 wt% WC composite coating exhibit the minimum wear rate.
- 4) The addition of particles into the polymer phase does not sacrifice the corrosion resistance of the polymer itself.
- 5) Xylan 1810 polymer exhibits better erosion-corrosion resistance than its composite coatings.
- 6) Xylan 1810 polymer also exhibits better erosion-corrosion resistance than GemThane and Al_2O_3 reinforced GemThane coatings.

5.2 RECOMMENDATIONS FOR FUTURE WORK

The coating quality is related to the coating texture or surface morphology. Therefore, the dispersion of larger particles either Al₂O₃ or WC particles (i.e. 300 nm) in the polymer matrix should be as uniformed as the nanoparticles composite coating (i.e. 50 nm Al₂O₃ particles).

The polymer and its composite coatings should be cast and left in the saline solution in order to quantify the water resistance of the coatings (such as measuring the water absorbance of the coatings).

Structural information on cross-linking is needed in order to fully understand the bonding mechanism between particle and polymer. Various analytical techniques such as FTIR and NMR can be used for this reason.

Different material of particles (i.e. metal / glass) should be used in order to justify if the properties of particles themselves would affect the composite material.

REFERENCES

ASTM D 823-95, Standard practices for producing films of uniform thickness of paint, varnish, and related products on test panels, 1995.

ASTM D 4060-95, Standard test method for abrasion resistance of organic coatings by the Taber Abraser, 1995.

Armstrong R.D. (2001). "Plasticity: Grain Size Effect". Encyclopedia of Materials: Science and Technology. Retrieved January 29, 2003, from The Encyclopedia of Materials: Science and Technology database. Available from the University of Alberta Library Web site:

<http://www.library.ualberta.ca/databases/databaseinfo/index.cfm?ID=2169>

Belaroui K., Rapillard G., Bowen P., Hofmann H., Shklover V., "Nanocrystalline Coating by Electrophoretic Deposition (EPD)", Key Engineering Materials, vol. 206-213, p519-522, 2002.

Biest V.D., Vandeperre L.J., "Electrophoretic Deposition of Materials", Annu. Rev. Mater. Sci., 29, p327-352, 1999.

Bradford S. A., "Corrosion Control", Van Nostrand Reinhold, New York, 1993.

Briscoe B.J., "Isolated contact stress deformations of polymers: the basis for interpreting polymer tribology", Tribology International, vol 31, No 1-3, p121-126, 1998.

Briscoe B.J., Evans P.D., Pelillo E., Sinha S.J., "Scratching maps for polymers", Wear, 200, p137-147, 1996.

Briscoe B.J., "Wear of Poly(tetrafluoroethylene)", Polymer Wear and Its Control, ACS Symposium Series 287, ed. Lee L.H., p151-170, 1985.

Briscoe B.J, "Wear of polymers: an essay on fundamental aspects", 3rd International Conference on the Wear of Materials, San Francisco, 1981.

Bhushan B. and Gupta B.K., "Handbook of Tribology", McGraw-Hill, 1991.

Bunshah R. F., "Handbook of Hard Coatings", Noyes Publications, New York, 2001.

Bunshah R.F., "HandBook of Deposition Technologies for Films and Coatings", 2nd edition, Noyes Publications, New York, 1994.

Cabot B. and Foissy A., "Reversal of the surface charge of a mineral powder: application to electrophoretic deposition of silica for anticorrosion coatings", Journal of Materials Science, 33, p3945-3952, 1998.

Crawmer D.E., "Plasma Spray Coatings", Encyclopedia of Materials: Science and Technology. Retrieved February, 2002, from The Encyclopedia of Materials: Science and Technology database. Available from the University of Alberta Library Web site: <http://www.library.ualberta.ca/databases/databaseinfo/index.cfm?ID=2169>

Crossen J.D., Sykes J.M., Briggs G.A.D., Lomas J.P., " Studies of Adhesion and Disbonding of Coatings by Scanning Acoustic Microscopy", Organic Coatings for Corrosion Control, ACS Symposium Series 689, ed. Bierwagen G.P., p106-122,1998.

Dahotre N.B., Kadolkar P., Shah S., "Refractory ceramic coatings: processes, systems and wettability/adhesion", Surf. Interface Anal., 31, p659-672, 2001.

Easterling K., "Introduction to the Physical Metallurgical of Welding", Butterworths, London, p35, 1983.

Gangal S.V.(2001). "Perfluorinated Polymers, Polytetrafluoroethylene", Encyclopedia of Polymer Science and Technology. Retrieved May 15, 2003, from The Encyclopedia of Polymer Science and Technology database. Available from the University of Alberta Library Web site:

<http://www.library.ualberta.ca/databases/databaseinfo/index.cfm?ID=3056>

Gong D., Zhang B., Xue Q.J., Wang H.L., "Investigation of Adhesion Wear of Filled Polytetrafluoroethylene by ESCA, AES and XRD", *Wear*, 57, p25-39, 1990.

Goren-Muginstein G.R., Berger S. , Rosen A., "Sintering Study of Nanocrystalline Tungsten Carbide Powders" *Nanostructured Materials*, 10(5), p795-804, 1998.

Habig K.H., "Chemical vapor deposition and physical vapor deposition coatings: Properties, tribological behavior, and applications", *J. Vac. Sci. Technol. A*, 4(6), p2832-2843, 1986.

Kijima K., Noguchi H., Konishi M., "Sintering of ultrafine SiC powders prepared by plasma CVD", *J. Mater. Sci.*, 24, p2929, 1989.

Kim H.J., Lee J.H., Sohn I.H., Hwang T.J., Lee K.Y., "Preparation of tungsten metal film by spin-coating method", *Korea-Australia Rheology Journal*, 14(2), p71-76, June 2002.

Klabunde K.J., Stark J., Koper O., Mohs C., Park D.G., Decker S., Jiang Y., Lagadic I., Zhang D.J., "Nanocrystals as Stoichiometric Reagents with Unique Surface Chemistry", *J. Phys. Chem.*, 100, p12142-12153, 1996.

Knox E.M., Cowling M. J., "Durability Aspects of Adhesively Bonded Thick Adherend Lap Shear Joints", *International Journal of Adhesion and Adhesives*, 20, p323-331, 2000.

Koch C.C., (2001). "Nanocrystalline Materials: Mechanical Properties", Encyclopedia of Materials: Science and Technology. Retrieved March 15, 2003, from The Encyclopedia of Materials: Science and Technology database. Available from the University of Alberta Library Web site:

<http://www.library.ualberta.ca/databases/databaseinfo/index.cfm?ID=2169>

Kunst H. et al., (2000). "Metals, Surface Treatment", Ullmann's Encyclopedia of Industrial Chemistry. Retrieved November 1, 2002, from Ullmann's Encyclopedia of Industrial Chemistry database. Available from the University of Alberta Library Web site: <http://www.library.ualberta.ca/databases/databaseinfo/index.cfm?ID=1131>

Li F., Hu K., Li J., Zhao B.Y., "The friction and wear characteristics of nanometer ZnO filled polytetrafluoroethylene", *Wear* 249, p877–882, 2002.

Lin L., Blackman G.S., Matheson R.R., "Quantitative characterization of scratch and mar behavior of polymer coatings", *Materials Science and Engineering A*, 317, p163–170, 2001.

Livne Z., Munitz A., Rawersa J.C., Fieldsb R.J., "Consolidation of Nanoscale Iron Powders", *NanoStructured Materials*, 10(4),p503-522, 1998.

Massimo G., "Sol-Gel Coatings on Metals", *Journal of Sol-gel Science and Technology*, 8, p443-449, 1997.

Masumura R.A., Hazzledine P.M., Pande C.S., "Yield Stress of Fine Grained Materials", *Acta Mater.*, 46(13), p4527-4534, 1998.

McFadden, S.X., Mishra R. S., Valiev R. Z., Zhilyaev A. P., Mukherjee A. K., "Low-temperature superplasticity in nanostructured nickel and metal alloys", *Nature*, 398, p684-686, 1999.

Mayo M.J., "High and low temperature superplasticity in nanocrystalline materials", *Nanostructured Materials*, 9(1-8), p717-726, 1997.

Neville A. and Hodgkiess T., "Study of effect of liquid corrosivity in liquid-solid impingement on cast iron and austenitic stainless-steel", *British Corrosion Journal*, 32(3), p197-205, 1997.

Ng C.B., Schadler L.S. and Siegel R.W., "Synthesis and mechanical properties of TiO₂-epoxy nanocomposites", *Nanostruct. Mater.*, 12, p507-510, 1999.

Pierson H.O., "Handbook of Chemical Vapor Deposition (CVD)", 2nd edition, Noyes Publication, New York, USA, 1999.

Pistor C. and Friedrich K., "Scratch and Indentation Tests on Polyoxymethylene (POM)", *Journal of Applied Polymer Science*, 66, p1985-1996, 1997.

Randall C. and Tassel J.V. (2001). "Electrophoretic Deposition", *Encyclopedia of Materials: Science and Technology*. Retrieved December 15, 2001, from The Encyclopedia of Materials: Science and Technology database. Available from the University of Alberta Library Web site:

<http://www.library.ualberta.ca/databases/databaseinfo/index.cfm?ID=2169>

Sarkar P., Datta S., and Nicholson P.S., "Functionally graded ceramic/ceramic and metal/ceramic composites by electrophoretic deposition", *Composites Part B*, 28B, p49-56, 1997.

Schwartz C.J. and Bahadur S., "Studies on the tribological behavior and transfer film-counterface bond strength for polyphenylene sulfide filled with nanoscale alumina particles", *Wear* 237, p261-273, 2000.

Simovic K., Miskovic-Stankovic V.B., Kicevic D., Jovanic P., "Electrophoretic deposition of thin alumina films from water suspension", *Colloids and Surfaces*, 209, p47-55, 2002.

Streckert H.H., Norton K.P., Katz J.D., Freim J.O., "Microwave densification of eletrophoretically infiltrated silicon carbide composite", *Journal of Materials Science* 32, 6429-6433, 1997.

Szycher M., "Handbook of Polyurethanes", CRC Press, Boca Raton, 1999.

Tanaka K. and Kawakami S., "Effect of Various Fillers on The Friction and Wear Of Polytetrafluoroethylene-based Composites", *Wear*, 79, p221-234, 1982.

Taylor S.R. (2001). "Coatings for Corrosion Protection: Organic", *Encyclopedia of Materials: Science and Technology*. Retrieved February 12, 2003, from The Encyclopedia of Materials: Science and Technology database. Available from the University of Alberta Library Web site:

<http://www.library.ualberta.ca/databases/databaseinfo/index.cfm?ID=2169>

Taylor S.R. (2001). "Coatings for Corrosion Protection: An Overview", *Encyclopedia of Materials: Science and Technology*. Retrieved February 12, 2003, from The Encyclopedia of Materials: Science and Technology database. Available from the University of Alberta Library Web site:

<http://www.library.ualberta.ca/databases/databaseinfo/index.cfm?ID=2169>

Uhlmann D.R., Teowee G., Boulton J., "The Future of Sol-Gel Science and Technology", *Journal of Sol-Gel Science and Technology*, 8, p1083-1091, 1997.

Vandeperre L., Biest O.V.D., "Electrophoretic Forming of Silicon Carbide Laminates with Graphite Interfaces", *Proc. 4th Euro Ceramics*, vol. 1, ed C. Galassi F. E., p359-366, 1995.

Wahl G. et al. (June 15, 2000). *Thin Films*, Ullmann's Encyclopedia of Industrial Chemistry. Retrieved October 7, 2002, from Ullmann's Encyclopedia of Industrial Chemistry database. Available from the University of Alberta Library Web site:

<http://www.library.ualberta.ca/databases/databaseinfo/index.cfm?ID=1131>

Wang C.B., Wang D.L., Chen W.X., Wang Y.Y., "Tribological properties of nanostructured WC/CoNi and WC/CoNiP coatings produced by electro-deposition", *Wear*, 253, p563–571, 2002.

Wang Q., Xue Q., Liu H., Shen W., Xu J., "The effect of particle size of nanometer ZrO on the tribological behaviour of PEEK", *Wear*, 198, p216–219, 1996.

Wang Q., Xue Q., Shen W., "The friction and wear properties of nanometre SiO₂ filled polyetheretherketone", *Tribol. Int.* 30 (3), p193–197, 1997.

Wang Z.L., "Characterization of Nanophase Materials", *Particle & Particle Systems Characterization*, 18(3), p142-165, October 2001.

Wetzel B., Hauptert F., Friedrich K., Zhang M. Q., Rong M.Z., "Impact and Wear Resistance of Polymer Nanocomposites at Low Filler Content", *Polymer Engineering And Science*, 42(9), p1919-1927, September 2002.

Windes W.E., Zimmerman J., Reimanis I.E., "Electrophoretic deposition applied to thick metal-ceramic coatings", *Surface and Coating Technology*, 157, p267-273, 2002.

Xiang C., Sue H.J., Chu J., Coleman B., "Scratch Behavior and Material Property Relationship in Polymers", *Journal of Polymer Science: Part B: Polymer Physics*, 39, p47-59, 2001.

Xu Y.M. and Mellor B.G., "The effect of fillers on the wear resistance of thermoplastic polymeric coatings", *Wear*, 251, p1522–1531, 2001.

Zarzycki J., "Past and Present of Sol-Gel Science and Technology", *Journal of Sol-Gel Science and Technology*, 8, p17-22, 1997.

Zhang S.L., Tsou A.H., Li J.C.M., "Friction and Damage in the Scratching of Poly(n-butyl acrylate) Films", *Journal of Polymer Science: Part B: Polymer Physics*, 40, p585-592, 2002.

Zhang S.W., Wang D., Yin W.H., "Investigation of abrasive erosion of polymers" *Journal of Materials Science*, 30, p4561-4566, 1995.

Zhu Y.C., Yukimura K., Ding C.X., Zhang P.Y., "Tribological properties of nanostructured and conventional WC-Co coatings deposited by plasma spraying", *Thin Solid Films*, 388, p277-282, 2001.